Journal of Engineering Advancements

Editor-in-Chief:

Prof. Dr. Mohammad Mashud

Volume 01 Issue 01

Journal of Engineering Advancements

Preface

I am very much pleased and delighted to introduce a new peer reviewed and open access journal, *Journal of Engineering Advancemen*ts (JEA), published by SciEn Publishing Group which is the first journal from the publisher in the field of engineering and applied sciences, and it is my great pleasure to be the Editor-in-Chief of the journal. Hope, the JEA will provide the perfect opportunity to explore oneself in the advancements of the fast growing field of study and to publish in a journal which has the outstanding outstretch and expectations of a significant impact.

The aims of this journal is to be the frontline international journal in the field of engineering and applied sciences. The journal will incorporate latest developments & trends, exclusive, and authentic contributions-research articles, reviews, and combinations as well as book and conference reviews. The JEA is served by a very potential and dynamic editorial board along with a network of academic and scientists from all around the world and different disciplines serving to assure superior contributions. The submission and review process of this journal is entirely online based. After submission of a paper to the website, authors will receive acknowledgement e-mail and two reviewers will be contacted. As soon as the reviewer comments are received by the editor, corresponding author will be notified through e-mail to entertain all reviewer comments. After the paper has been accepted, editing and formatting will be done by the publisher. Editorial team will ensure the legitimacy of this journal by practicing to be transparent to the authors and researchers.

I appreciate and deeply grateful of the editorial team for their efforts to take initiative and establish such kind of resourceful standard journal. Finally, from myself, the editorial board members and publisher, I like to convey our gratitude and thanks to the authors and reviewers.

I am looking forward to the submission of high quality articles in this journal.

Best wishes and thanks in advance for your contribution to the *Journal of Engineering Advancements.*

Prof. Dr. Mohammad Mashud
Editor-in-Chief

Journal of Engineering Advancements

CONTENTS

Original Articles

Compressive Properties of Expanded Perlite Based Particulate Composite for the Application in Building Insulation Board

Partho Adhikary[1], Md Arifuzzaman[2,] and Emamul Kabir[2]*

[1]Department of Biomedical Engineering, Khulna University of Engineering & Technology, Khulna-9203, BANGLADESH
[2]Department of Mechanical Engineering, Khulna University of Engineering & Technology, Khulna-9203, BANGLADESH

ABSTRACT

In this paper, expanded perlite based particulate composites for the application in building insulation board are studied for compressive behaviour. Composites with a density range from 0.452 to 0.640 g/cm^3 are manufactured using floatation method by varying binder content (sodium silicate solution and corn starch as binder) and the degree of compaction. Compressive strength and modulus are investigated based on two manufacturing parameters (i.e. Compaction ratio and Water/SSS ratio) and the density of the composites. Compressive strength and modulus were found to be linearly dependent on the density however the trend for compressive strength and modulus were found to be different. The change of compressive modulus with respect to increasing density is found to be different for different compaction ratio which is not significant in the case of compressive strength. The range of specific compressive strength of the composites from 4.27 to 5.08 MPa/(g/cm^3) was found to be suitable for the building insulation board application when compared with existing literature.

Keywords: Expanded Perlite; Sodium Silicate Solution; Corn Starch; Building Insulation Board; Compressive Strength; Compressive Modulus.

1. Introduction

Perlite is typically made by the hydration of obsidian [1] and can be expanded to form cellular structure [2], [3]. The expansion can be done at a temperature of 649-816 ^{0}C with the removal of water molecules [4]. Expanded perlite [5]-[7] particles are porous, lightweight, fire resistant, insulator to sound and heat, chemically inert and cheap. In applications for interior walls and ceilings, the thermal conduction is important for energy saving during heating and cooling and the weight of a material is a significant factor for transportation and installation because of the large amount of material to be handled. So, expanded perlite particles may be a potential constituent material for the development of such building material because of its lightweight and low cost. Researchers have been working on expanded perlite particle based building boards such as perlitic insulation board by Hill [8], building boards made of fibre/asphalt coated perlite by Miscall and Rahr [9], mineral board by Sherman and Cameron [10], perlite/starch composite by Shastri and Kim [11], gypsum/perlite composites by Vimmrova [12], Perlite/sodium silicate composite by Arifuzzaman and Kim [13] etc. However there is an enormous scope to develop perlite based building materials with the use of more cheap and easily available binding materials such as corn starch as a reinforcement to sodium silicate solution. Sodium silicate solution is fire resistant and corn starch is a good binder.

Therefore, the objectives of this paper are to consolidate perlite based particulate composites using the novel floatation method [11] with the use of gelatinized corn starch as a reinforcement to sodium silicate solution, to investigate compressive properties of the composites and to find the suitability of the composite for building board applications.

2. Materials and method

2.1 Expanded perlite

Expanded perlite particles are purchased from China and separated into various particle size groups (1-2 mm, 2-3 mm and 3-4 mm) using sieves. Particle size group 3-4 mm were chosen for this work. According to the data sheet provided by the manufacturer expanded perlite contained 71-74% Silicon Oxide, 12-13% Aluminium Oxide, 3-4% Sodium Oxide, 3-5% Potassium Oxide, 1.2% Calcium Oxide, 1.0% Ferric Oxide and some diminutive amount of Titanium Oxide and Magnesium Oxide. The bulk density of perlite particles was measured using a measuring cylinder of 100 cm^3 capacity into which particles were first poured slowly with a spoon. Then the mass of particles were recorded. The bulk density of the expanded perlite was calculated using the equation

Bulk density, ρ = (the mass of perlite particles / the volume of perlite particles) g/cm^3.   (1)

The average bulk density of 3-4 mm perlite particles was found to be 0.187 g/cm^3.

2.2 Sodium silicate solution (SSS) and starch

Sodium silicate solution was used as a binder having a density of 1.39 g/cm^3. It is necessary to determine the solid content of sodium silicate solution after dehydration to properly characterize it for reproducibility of results. SSS was diluted with drinking water at different ratio [See Table 1] and then stirred for 2-3 minutes. The diluted SSS of fixed mass are then dried inside an oven at 120^{0}C until no mass change is noticed.

The difference in mass of diluted SSS and solid sodium silicate after dehydration indicates the solid contents in diluted SSS. The solid contents for various Water to SSS ratios are given in Table 1. It is seen that the solid content is affected by dilution and decreased with increasing Water/SSS ratio. Solid content on SSS without dilution is found to be 48.60%.

**Table 1** Solid content in SSS with various dilution

Sample	Mass of SSS, g	Mass of water, g	Water to SSS ratio	Solid content in diluted SSS, %
01	5	0.0	0	48.60
02	5	5.0	1	26.70
03	5	10.0	2	19.80
04	5	15.0	3	14.50

To determine solid content in corn starch solution, 100g of water was taken into a beaker and different amount of starch powder was added to it and stirred the solution at above 70^0C for 30 minutes and a clear solution is obtained as a result of polymerization. After polymerization 20g solution was taken into an empty test tube and put it into an oven at 120^0C until there is no mass change due to water loss. The solid contents obtained for various starch content in water is given in Table 2 and in Fig. 1. It is seen that solid content increased linearly with increasing starch content in binder but not all starch powder are gelatinized for the set temperature and time in this work which is reflected in the loss percentage. The loss percentage indicates that only about 66.34% starch powder was gelatinized due to polymerization.

Table 2 Determination of solid content in Starch

Sample	Mass of Starch, g	Mass of water, g	Starch content in binder, %	Solid content, %	Loss, %
1	0.50	100	0.498	0.35	29.65
2	1.00	100	0.990	0.65	34.35
3	1.50	100	1.478	0.95	35.72
4	2.00	100	1.961	1.25	36.25
5	2.50	100	2.439	1.65	32.35

An analogous procedure was followed to measure the solid content in combined solution i.e. diluted sodium silicate solution with starch powder according to the combination given in Table 3. SSS was added to gelatinized starch for making combined solution. The solid content in the prepared solution is also found to be decreased with increasing Water/SSS ratio but the solid content in the combined solution is slightly higher due to the addition of starch.
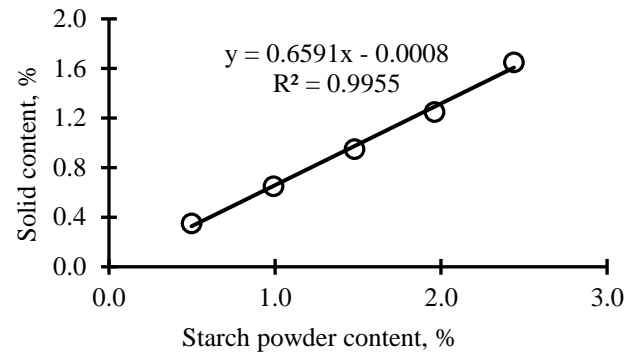
Fig. 1 Solid content in the gelatinized starch solution as a function of starch powder in water

Table 3 Determination of solid content in SSS + Starch

Sample	Mass of starch, g	Mass of water, g	Mass of SSS, g	Water/SSS ratio	Solid content, %
1	1.50	100	100.00	1	28.10
2	1.50	100	50.00	2	22.10
3	1.50	100	33.33	3	16.85
4	1.50	100	25.00	4	12.60

2.3 Specimen preparation process

The process of manufacturing composite consists of binder preparation, mixing, compaction, and drying steps. The binder is prepared by mixing a fixed amount of corn starch (see Table 3 for mix proportion) with water and then continuously stirring at 70^0C for 30 minutes for gelatinization. Later SSS was added to the gelatinized solution according to Table 4. A PVC pipe having diameter 42 mm was taken and one side of the opening was blocked by a plastic wire net. Then different mass of expanded perlite particle for different compaction ratio (Compaction ratio = the ratio of the volume of perlite before compaction and final specimen volume) was poured into the PVC pipe. The required expanded perlite mass was calculated using equation

Mass of perlite particle required = bulk density of perlite × specimen final volume × compaction ratio.   (2)

The PVC pipe with expanded perlite is dipped and soaked into the binder solution until all perlite particle get wet before transferring the PVC mould for compaction. During compaction, 2/3 of compaction stroke was applied from the top side and rest from bottom side of the mould to obtain uniform density through the thickness. The specimen was removed from the mould by pushing with the plunger. The specimen was kept on a paper towel and performed a frequent shifting of specimen to ensure there is no binder in the towel. Then the wet mass of the specimen was taken and transferred into an oven for drying at 120°C for 24 hours. The dry mass was recorded when the specimen reached room temperature. At least three test specimens were prepared for each combination of compaction ratios (i.e. 2.5, 3.0 and 3.5) and Water to SSS ratios (i.e. 1, 2, 3, and 4).

Table 4 Density, compressive strength and compressive modulus of manufactured composites for various combinations of compaction ratios and Water to SSS ratios.

Water/SSS ratio	Density, g/cm³			Compressive strength, MPa			Compressive modulus, MPa		
	C.R= 2.5	C.R.= 3.0	C.R.= 3.5	C.R= 2.5	C.R.= 3.0	C.R.= 3.5	C.R= 2.5	C.R.= 3.0	C.R.= 3.5
1	0.478	0.538	0.640	2.23	2.53	3.25	21.22	33.15	54.89
2	0.470	0.510	0.607	2.12	2.44	3.04	32.87	37.29	49.13
3	0.463	0.491	0.578	2.04	2.32	2.82	37.54	43.26	47.67
4	0.452	0.480	0.554	1.93	2.23	2.48	48.44	46.23	44.34

2.4 Density measurement

The final height, diameter and mass of the specimen was measured to calculate the density using the equation,

Density = Final mass of the specimen / the volume of the specimen. (3)

2.5 Compression test

The compression test was carried out in the Universal Testing Machine with a load cell of capacity 50 kN and digital data acquisition system at a displacement rate of 5 mm/min. At least three specimens were tested. The compressive strength was calculated using the equation

Compressive strength = Peak force / cross sectional area of the specimen. (4)

The compressive modulus was measured from the slope of the most linear part of the stress versus strain curve before peak load.
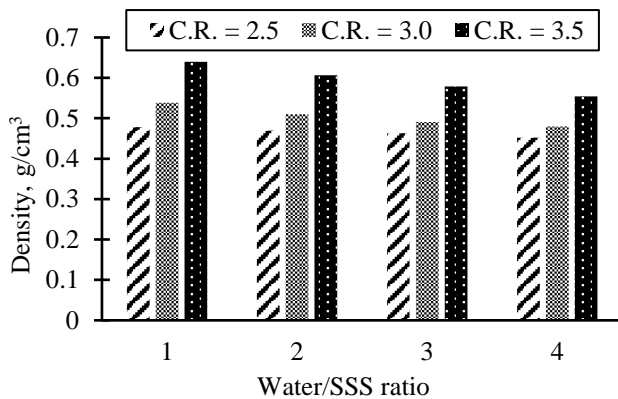
Fig. 2 Density of the manufactured composites for various combinations of compaction ratios and Water/SSS ratios

3. Results and discussion

The physical and mechanical properties of the manufactured composites for various combinations of compaction ratios and Water/SSS ratios are listed in Table 4. Density is plotted as a bar chart for various Water/SSS ratio and compaction ratio in Fig. 2. It is observed that the density of the composites increased with increasing compaction ratio for all Water/SSS ratio expectedly because higher compaction means higher amount of perlite and binder in the composites. On the other hand, for a constant compaction ratio, the density of the composites showed a decreasing trend when Water/SSS ratio

increased for all compaction ratio (see Table 4). A high Water/SSS ratio indicates less amount of solid in the binder (see Table 4) which reduced the density of the specimens for fixed amount of perlite.
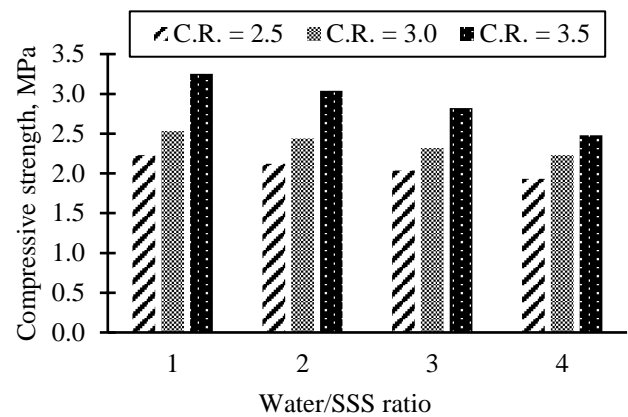
Fig. 3 Compressive strength of the manufactured composites for various combinations of compaction ratios and Water/SSS ratios.

Compressive strength of composites are plotted in Fig. 3 to see the effect of Water/SSS ratio and compaction ratio. The compressive strength increased with increasing compaction ratio for all Water/SSS ratio and it decreased with increasing Water/SSS ratio for all compaction ratio. For a constant Water/SSS ratio, when compaction ratio is increased the pores of cellular perlite particles are reduced which causes an increase in compressive strength. Since the increase in Water/SSS ratio for a constant compaction ratio reduces the amount of binder in the composite, it causes the reduction of load carrying capacity of the composite and hence compressive strength decreased.

A bar chart is plotted in Fig. 4 for compressive modulus of manufactured composites to investigate the effect of Water/SSS ratio and compaction ratio. The compressive modulus appeared to increase with increasing compaction ratio for Water/SSS ratio = 1 to 3 but for Water/SSS ratio 4 the trend is reversed. As the Water/SSS ratio increased from 1 to 3, the rate of increase in compressive modulus is decreased and become negative when Water/SSS ratio = 4. On the other hand, compressive modulus increased with increasing Water/SSS ratio for compaction ratio 2.5 and 3.0 but for compaction ratio 3.5 it decreased. The highest compressive modulus is notices for composite with compaction ratio=3.5 and Water/SSS ratio=1. For compaction ratio 2.5 and 3.0, the lesser the binder content in the composite the higher the compressive modulus and the rate of increase in compressive

modulus with increasing Water/SSS ratio is decreased when compaction ratio is increased from 2.5 to 3.0. Therefore the rate of increase in compressive modulus with decreasing binder content is suppressed with increased compaction ratio and as part of the continuation of suppression the rate become negative at compaction ratio 3.5.
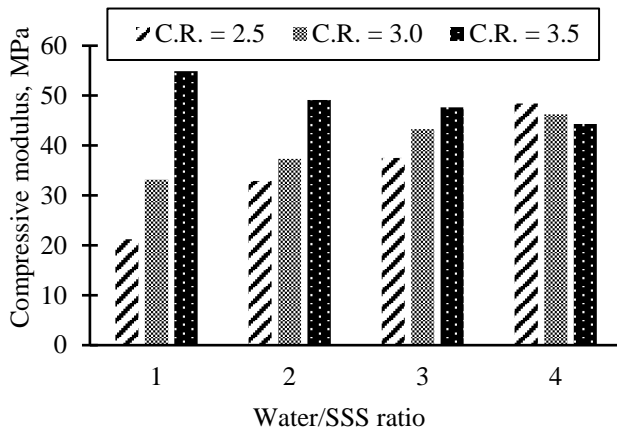
Fig. 4 Compressive modulus of the manufactured composites for various combinations of compaction ratios and Water/SSS ratios.

Fig. 5 Compressive strength of the composites as a function of density for various compaction ratios

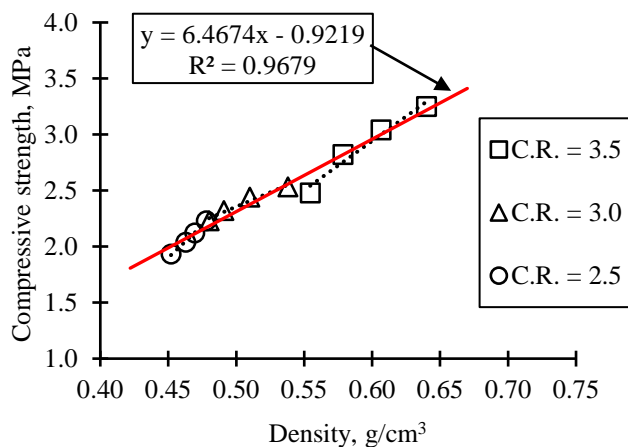Compressive strength is plotted as a function of density for various compaction ratio in Fig. 5. It is observed that compressive strength increased linearly with increasing density for all compaction ratio and the higher compaction ratio results higher compressive strength. The least square line and correlation coefficient (R^2) were y = 11.468x − 3.2598 and 0.9934 for C.R. = 2.5; y = 5.1402x − 0.2143 and 0.9599 for C.R. = 3.0; and y = 8.7715x − 2.3207 and 0.9635 for C.R. = 3.5. It is also interesting to see that compressive strength increased linearly with increasing density with least square line y = 6.4674x-0.9219 and correlation coefficient R^2 = 0.9679 irrespective to the compaction ratio. The high correlation coefficient indicates high linearity. So, it is apparent that the compressive strength is dependent on the density of the composite material although the density of the composite itself is a function of the manufacturing parameters as discussed earlier.

Compressive modulus is given as a function of density for various compaction ratio in Fig. 6. Compressive modulus decreased linearly with increasing the density of the composite for compaction ratio 2.5 and 3.0 but it showed an opposite trend for compaction ratio 3.5. The least square lines and correlation coefficients (R^2) are y = -1021.6x +510.68 and 0.993 for C.R. = 2.5; y= -227.94x+155.04 and 0.984 for C.R. = 3.0; and y = 117.12x- 20.66 and 0.980 for C.R. = 3.5. It is also observed that the rate of decrease in compressive modulus lessened when compaction ratio increased from 2.5 to 3.0 and to follow the trend eventually at compaction ratio 3.5 the compressive modulus increased linearly with increasing the density.
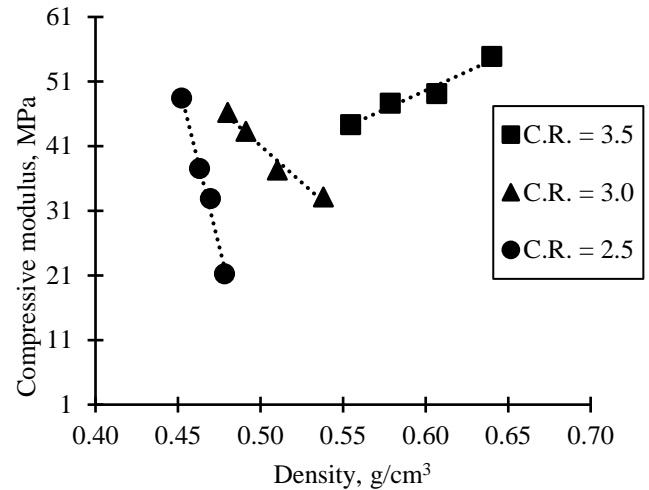
Fig. 6 Compressive modulus of the composites as a function of density for various compaction ratios

Now, it is necessary to outline compressive properties along with the density of some building board materials available in the literature for the purpose of comparison. Colak [14] reported a range of specific compressive strength of building board from 0.62 to 2.03 MPa/(g/cm^3), Arifuzzaman and Kim [13] showed a range from 0.8 to 5.37 MPa/(g/cm^3), Skujans et al. [15] found a range from 1.1 to 3.1 MPa/(g/cm^3) and Vimmrova et al. [12] stated a range from 1 to 3.86 MPa/(g/cm^3) which are highly comparable with the current composites with a range from 4.27 to 5.08 MPa/(g/cm^3). So, the composites that are studied here are suitable for application in building insulation board.

4. Conclusions

Expanded perlite based particulate composites with a range of density from 0.452 to 0.640 g/cm^3 were manufactured by varying the degree of compaction and binder contents to study compressive properties. Compressive strength and modulus are analysed based on manufacturing parameters (i.e. Compaction ratio and Water/SSS ratio) and the density of the composites. Compressive strength is found to be increased with increasing compaction ratio, binder content and the density of composites. Compressive modulus decreased with increasing density for low compaction ratio but at high compaction ratio it showed an increasing trend. The composites were found to be suitable for building board applications based on the range of specific compressive strength from 4.27 to 5.08 MPa/(g/cm^3) when compared with available literature.

References

[1] Luongo JS, inventor; Advanced Construction Materials Corp, assignee. Strengthened, light weight wallboard and method and apparatus for making the same. United States patent US 6,251,979. 2001 Jun 26.

[2] Yilmazer S, Ozdeniz MB. The effect of moisture content on sound absorption of expanded perlite plates. Building and Environment. 2005 Mar 1;40(3):311-8.

[3] Dube WP, Sparks LL, Slifka AJ. Thermal conductivity of evacuated perlite at low temperatures as a function of load and load history. Cryogenics. 1991 Jan 1;31(1):3-6.

[4] Reka AA, Pavlovski B, Lisichkov K, Jashari A, Boev B, Boev I, Lazarova M, Eskizeybek V, Oral A, Makreski P. Chemical, mineralogical and structural features of native and expanded perlite from Macedonia. Geologia croatica. 2019 Oct 31;72(3):215-21.

[5] Singh M, Garg M. Perlite-based building materials—a review of current applications. Construction and Building Materials. 1991 Jun 1;5(2):75-81.

[6] Burriesci N, Arcoraci C, Antonucci P, Polizzotti G. Physico-chemical characterization of perlite of various origins. Materials Letters. 1985 Jan 1;3(3):103-10.

[7] Johnstone SJ. Minerals for the chemical and allied industries. Geological Magazine. 1954 Oct;91(5):408-9.

[8] Hill JA, inventor; Johns Manville Corp, assignee. Perlitic insulating board. United States patent US 4,126,512. 1978 Nov 21.

[9] Jack M, Rahr CE, inventors; SGL Carbon Corp, assignee. Building board of fiber and asphalt coated perlite. United States patent US 2,626,864. 1953 Jan 27.

[10] Sherman N, Cameron JH, inventors; Conwed Corp, assignee. Method of manufacturing improved mineral board. United States patent US 4,297,311. 1981 Oct 27.

[11] Shastri D, Kim HS. A new consolidation process for expanded perlite particles. Construction and Building Materials. 2014 Jun 16;60:1-7.

[12] Vimmrova A, Keppert M, Svoboda L, Černý R. Lightweight gypsum composites: Design strategies for multi-functionality. Cement and Concrete Composites. 2011 Jan 1;33(1):84-9.

[13] Arifuzzaman M, Kim HS. Novel mechanical behaviour of perlite/sodium silicate composites. Construction and Building Materials. 2015 Sep 15;93:230-40.

[14] Colak A. Density and strength characteristics of foamed gypsum. Cement and Concrete Composites. 2000 Jun 1;22(3):193-200.

[15] Skujans J, Vulans A, Iljins U, Aboltins A. Measurements of heat transfer of multi-layered wall construction with foam gypsum. Applied Thermal Engineering. 2007 May 1;27(7):1219-24.

Comparative Study on Mechanical Properties of Bamboo Strip and Bamboo Strip-Glass Fiber Reinforced Hybrid Composites

Mahir Asif, Kazi Adnan Rahman, Mohammad Omar Faisal and Md. Shariful Islam*

Department of Mechanical Engineering, Khulna University of Engineering & Technology, Khulna-9203, BANGLADESH

ABSTRACT

In this paper, mechanical properties of bamboo strip and bamboo strip-glass fiber reinforced hybrid composite were investigated. Composites were manufactured by using hand lay-up technique and bamboo strips were made from locally available bamboo. Four layers of bamboo strip composite were manufactured and in case of hybrid composite, two layers of glass fiber one at the top and the other at the bottom were used with the aim was to observe the effect of adding glass fiber layer on the mechanical properties of bamboo strip composite. Tensile and flexural properties were studied and it was found that adding the glass fiber layer doesn't have any significant effect on tensile properties but flexural strength and modulus have increased by 22.49 % and 15.02 % respectively.

Keywords: Bamboo Strip; Hybrid Composite; Tensile Strength; Flexural Strength.

1. Introduction

Fiber-reinforced plastic (FRP) is a thermoset polymer composite material which is made of a polymer matrix reinforced with fibers. Based on the source, fibers are divided mainly into two categories: natural and synthetic. The natural fibers such as cellulose fiber, wood fiber, flax, hemp, silk, jute, sisal, kenaf, cotton, and synthetic fibers such as glass, carbon, or aramid so on are being used to reinforce thermoplastics and thermosets by many researchers. Epoxy, vinyl ester, or polyester thermosetting plastic are used as the polymer matrix. Fiber-reinforced polymer composites are commonly used in the aerospace, automotive, marine, and construction industries [1]. The usage of FRP composites continues to grow at a staggering rate, and they are introduced in fields such as biomedical devices and civil structures [2]. This boom is due to the development of new advanced forms of FRP materials, which include high-performance resin systems and developed styles of reinforcement [2]. Properties such as lightweight, no-corrosive, exhibit high specific strength and specific stiffness, simple manufacturing process are the reasons FRP is becoming popular day by day.

Natural fibers have many favorable mechanical properties such as low abrasion resistance, low density, high toughness, acceptable specific strength properties, excellent thermal properties, enhanced energy recovery, biodegradability [3], acceptability, and so on [4]. Because of their ecofriendly nature and sustainability, natural fibers are getting attention from researchers and academicians to utilize in polymer composites. Various chemical treatments have been used successfully in enhancing the mechanical properties of natural fibers to overcome noticeable drawbacks in fiber nature [5]. On the other hand, synthetic fibers have been used in research and commercial purposes [6]. High-performance synthetic composites are used to reduce weight in automotive, aerospace, and other transport applications. Thus, savings in running costs are ensured, and more significantly, carbon emission is reduced, helping to increase resource efficiency and drive our shift to low carbon vehicles.

Bamboo is an abundant natural resource found in Asia, which is used for structural purposes, e.g., building houses, making temporary bridges in rural areas from ages [7]. It has the fastest growth rates amongst the natural fibers. It grows to its fullest within 6-8 months [8]. Besides, bamboo fibers contain 60% cellulose, a considerably high percentage (32%) of lignin [9]. These lignocellulosic fibers are capable of imparting high strength in materials. Also, bamboo fiber-reinforced composites have low density, high specific strength, fewer health hazards, less machine wear during processing. Most significantly, the costs of bamboo species are very low per unit volume, and consequently, the production cost can be reduced to a great extent. So, bamboo can be used as a reinforcing agent in composite material. Among the synthetic fibers, glass fibers - based on silica (SiO_2) with additions of oxides of calcium, boron, iron, and aluminum - are the most common reinforcement used in various applications to replace more substantial metal parts. Although these fibers weigh more than carbon, their impact-resistant properties are better than carbon fiber. Depending upon the glass type, filament diameter, sizing chemistry and fiber form, a wide variety of features and performance levels can be obtained [10], but it is the different concentrations of metal oxides that allow different glass types to be produced.

Recent researches have been focused on the mechanical properties of natural fibers like jute, wood, coir, and bamboo. Lakkad et al. [11] and Jindal [11] reported on the mechanical properties of bamboo, and Pakotiprapha et al. [13] reported on the reinforcement of cement by bamboo fibers. Rajulu et al. [14] investigated the effect of fiber length on the tensile properties of short bamboo fiber epoxy composite. Chen et al. [8] investigated the mechanical properties of bamboo fiber-reinforced polypropylene and compared the results with those of commercial wood-pulp. Thwe et al. [15] investigated the effect of actual environmental aging on the mechanical properties of bamboo-glass fiber reinforced polymer hybrid composites.

This paper investigates the mechanical properties of bamboo strip composites and bamboo strip-glass fiber reinforced hybrid composites. The primary focus of this paper was to observe the effect of glass fiber layer on the mechanical properties of hybrid composites.
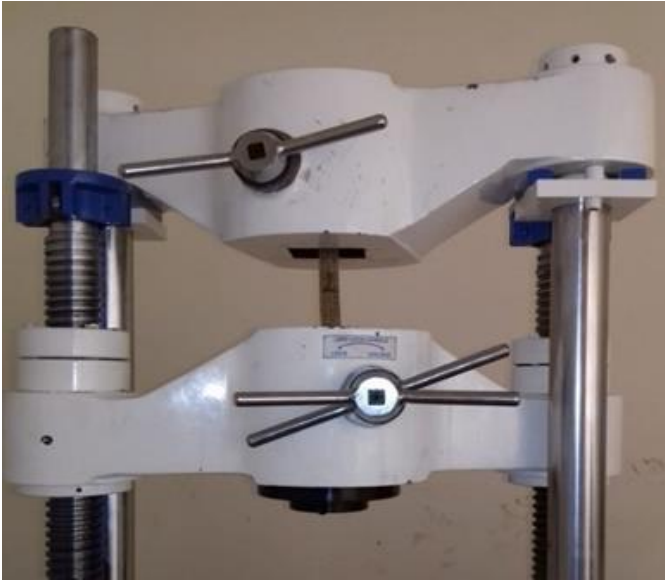
Fig. 1 Experimental setup for tensile test

2. Experimental Details

2.1 Materials

Bamboo strip and glass fiber was used as reinforcing material. The bamboo species used for the preparation of composites was *Bambusa Paravariabilis*, which grows abundantly in this part of Asia. Bamboo chips were cut using a wood planer, which were then ground into long strips manually by knives, and were then dried in sunlight for 3 days afterward. Otherwise, for hydrophilic behavior, bamboo strips would absorb moisture, which might affect the quality of the composite. Then the pieces were woven in a plain weave pattern to a 300×300 mm^2 square shape.

Fig. 2 Experimental setup for flexural test

On the other hand, non- woven, stitch-bonded cloth type glass fiber with a thickness of 0.03 mm was used. For the composite fabrication, epoxy resin and hardener were used. The hardener was mixed with the adhesive at a ratio of 1:10 as recommended by the manufacturer. This resin was chosen because of its accessibility and compatibility with natural fibers.
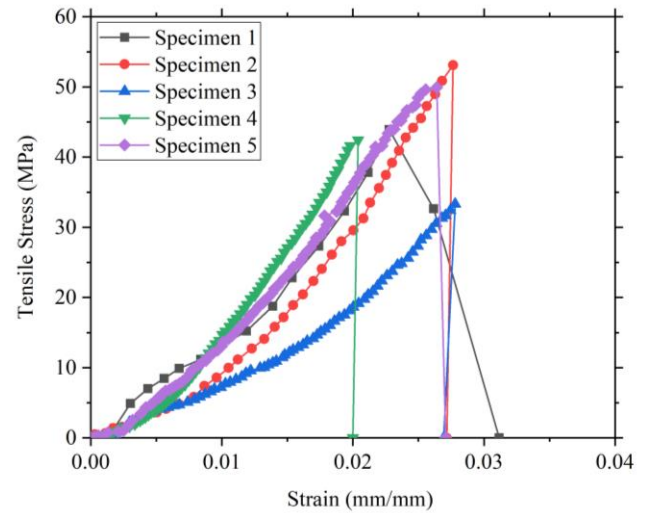
(a)
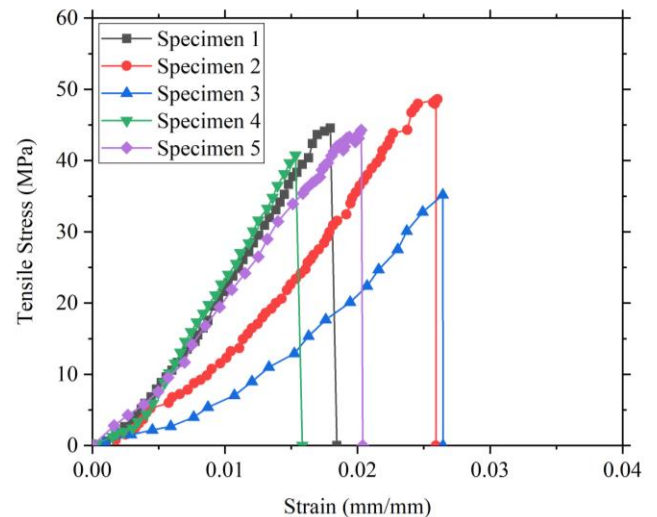
(b)

Fig. 3 Stress-strain diagram for the tensile test of (a) bamboo strip and (b) hybrid composite

2.2 Manufacturing Process

Manufacturing of the composite was done using the hand lay-up process. At first, the laminated composites with a total of four plies were manufactured with epoxy resin by hand lay-up technique. Rectangular stainless-steel plate with a size of 300 mm×300 mm was taken as a mold plate. Two stainless steel mold plate were used at the top and bottom of composite laminate during manufacturing of composites. At first, the bottom mold plate were positioned and on the top surface of that mold plate lubricating oil was brushed which acts as a mold release. The first layer of fiber was placed on top of the bottom mold plate. Resin was the poured on the first layer and the resin was uniformly distributed with the help of brush and roller. The

second layer of the fiber was placed on top of the first layer and similar procedure repeated for all the successive layer. Once all the fiber layer were placed and resin was poured and distributed evenly, top mold plate was then placed on top of the top fiber layer. Again, the bottom surface of the top mold plate was lubricated for the easy removal of composite after curing. A pressure of 1 MPa was applied evenly on the top mold plate and leave it for 24 hours for curing at room temperature. After curing, the composite laminate was removed and cut into pieces for tensile and flexural testing following the corresponding ASTM standard. Note that, for the manufacturing of bamboo composite, 4 layers of woven bamboo strips were used and for the hybrid composite, along with 4 layers of bamboo, 2 layers of glass fiber were placed on the top and bottom surfaces.

(a)

(b)

Fig. 4 Comparison of tensile properties of bamboo and hybrid composite (a) strength and (b) modulus

2.3 Tensile Test

Tensile tests in longitudinal directions of the manufactured bamboo strip composite and hybrid composite were conducted as per the ASTM D3039 standard [16]. Tensile test specimens were cut parallel to the fiber direction with the following dimensions: length 250 mm, width 25 mm. For each composite type, five identical samples were tested. The tensile test was conducted using a 2 mm/min crosshead speed. Fig. 1 shows the tensile test setup at the universal testing machine.

2.4 Flexural Test

Flexural tests were conducted on a three-point bending machine (refer to Fig. 2) following the ASTM D7264 standard [17]. Specimens of 125 mm length and 13 mm width were cut and were loaded in a three-point bending test with a recommended span-to-thickness ratio of 16:1. The specimen length was about 20 % longer than the support span. Five identical specimens were tested for each composite.

3. Results and Discussion

3.1 Tensile Test Results

Tensile tests were performed on five bamboo fiber reinforced composites and five bamboo-glass fiber reinforced hybrid composites. Fig. 3 shows the stress strain diagram for the tensile test. It is observed from Fig. 3 (a) that the maximum tensile stress for bamboo fiber composite varies from sample to sample while the maximum tensile stress for hybrid composites are more consistent.

(a)

(b)

Fig. 5 Stress-strain diagram for the flexural test of (a) bamboo strip and (b) hybrid composite

Fig. 4 shows the comparison of tensile strength and modulus of bamboo fiber and hybrid composite. It can be observed from this figure, that both the tensile strength and modulus remains almost constant for both composites which indicates that, adding glass fiber layers doesn't have significant effect on the tensile properties.

3.2 Flexural Test Results

Flexural tests were also performed on five bamboo strip and five hybrid composite specimen. Fig. 5 shows stress strain diagram for both bamboo strip and hybrid composite. It is observed from this figure, that the maximum stresses in Fig. 5 (b) compared to Fig. 5 (a) are higher which indicates that flexural strength for hybrid composite is higher compared to bamboo fiber reinforced composite. This can also be seen in Fig. 6 (a) which shows the flexural strength for hybrid composite is 22.49 % greater than bamboo fiber composite. It is also observed from Fig. 5 (b) that slope of the lines are stiffer than in Fig. 5 (a) which implies a greater flexural modulus for hybrid composite compared to bamboo fiber composite. Fig. 6 (b) confirms this statement which shows a 15.02 % increase in flexural modulus in case of hybrid composite.

(a)

(b)

Fig. 6 Comparison of flexural properties of bamboo and hybrid composite (a) strength and (b) modulus
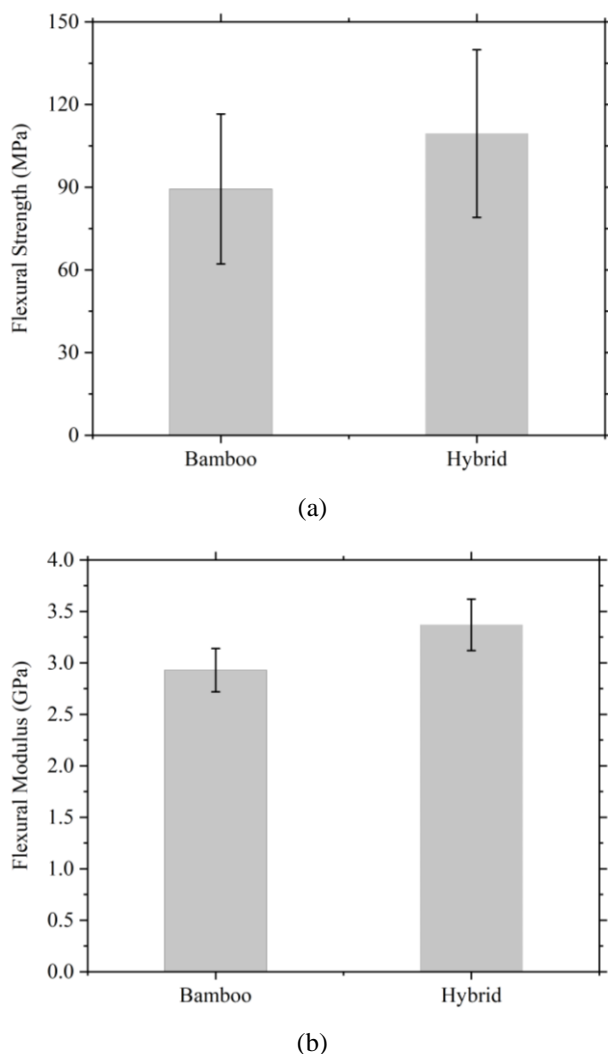
4. Conclusion

The comparative analysis of tensile and flexural properties of the bamboo fiber and bamboo-glass fiber composite was done. The results concluded that in the case of tensile properties, there is no significant change in the tensile strength and modulus. On the other hand, a 22.49 % increase in flexural strength and 15.02 % increase in flexural modulus was observed for hybrid composites. Since no significant effect in the tensile properties observed, the bamboo strip composite can be used where tensile strength is of primary concern i.e., the structural application like tension member in frames, whereas the hybrid composite can be used in bridges, column support where flexural strength is of greater interest.

References

[1] Jose JP, Thomas S, Kuruvilla J, Malhotra SK, Goda K, Sreekala MS. Advances in polymer composites: macro- and microcomposites—state of the art, new challenges, and opportunities. Polymer Composite: Macro-and Microcomposites. Weinheim: Wiley-VCH Verlag GmbH Co. KGaA. 2012;1:3-4.

[2] Tong L, Mouritz AP, Bannister MK. 3D fibre reinforced polymer composites. Elsevier; 2002 Nov 20.

[3] Herrera-Franco P, Valadez-Gonzalez A. A study of the mechanical properties of short natural-fiber reinforced composites. Composites Part B: Engineering. 2005 Dec 1;36(8):597-608.

[4] Shubhra QT, Alam AK, Quaiyyum MA. Mechanical properties of polypropylene composites: A review. Journal of thermoplastic composite materials. 2013 Apr;26(3):362-91.

[5] Liu D, McDaid AJ, Aw KC, Xie SQ. Position control of an ionic polymer metal composite actuated rotary joint using iterative feedback tuning. Mechatronics. 2011 Feb 1;21(1):315-28.

[6] Geethamma VG, Mathew KT, Lakshminarayanan R, Thomas S. Composite of short coir fibres and natural rubber: effect of chemical modification, loading and orientation of fibre. Polymer. 1998 Jan 1;39(6-7):1483-91.

[7] Shin FG, Xian XJ, Zheng WP, Yipp MW. Analyses of the mechanical properties and microstructure of bamboo-epoxy composites. Journal of Materials Science. 1989 Oct 1;24(10):3483-90.

[8] Chen X, Guo Q, Mi Y. Bamboo fiber- reinforced polypropylene composites: A study of the mechanical properties. Journal of applied polymer science. 1998 Sep 6;69(10):1891-9.

[9] Chattopadhyay SK, Khandal RK, Uppaluri R, Ghoshal AK. Bamboo fiber reinforced polypropylene composites and their mechanical, thermal, and morphological properties. Journal of applied polymer science. 2011 Feb 5;119(3):1619-26.

[10] Lawton EL, Wallenberger FT, Li H. Recent Advances in Oxide Glass Fiber Science. MRS Online Proceedings Library Archive. 2001;702.

[11] Lakkad SC, Patel JM. Mechanical properties of bamboo, a natural composite. Fibre science and technology. 1981 Jun 1;14(4):319-22.

[12] Jindal UC. Development and testing of bamboo-fibres reinforced plastic composites. Journal of Composite Materials. 1986 Jan;20(1):19-29.

[13] Pakotiprapha B, Pama RP, Lee SL. A study of bamboo pulp and fiber cement composites. InSymposium on Reduction of Housing Costs, Topic III 1978 (Vol. 220).

[14] Rajulu AV, Baksh SA, Reddy GR, Chary KN. Chemical resistance and tensile properties of short bamboo fiber reinforced epoxy composites. Journal of reinforced plastics and composites. 1998 Dec;17(17):1507-11.

[15] Thwe MM, Liao K. Effects of environmental aging on the mechanical properties of bamboo–glass fiber reinforced polymer matrix hybrid composites. Composites Part A: Applied Science and Manufacturing. 2002 Jan 1;33(1):43-52.

[16] ASTM D. 3039. Standard test method for tensile properties of polymer matrix composite materials. Annual book of ASTM standards. 2000;15:106-8.

[17] ASTM D7264.. Standard test method for flexural properties of polymer matrix composite materials. American Society for Testing and Materials Annual Book of ASTM Standards. 2007.

Numerical Analysis of Ratcheting Under Bending- Membrane Loading Conditions

Sajib Kumar Nath*, Md. Makfidunnabi and Md Abdullah Al Bari

Department of Mechanical Engineering, Khulna University of Engineering & Technology, Khulna-9203, BANGLADESH

ABSTRACT

Ratcheting is a vital failure mode when dynamic loading is present in the scenario and it can lead to fatigue or incremental collapse if not restricted. The purpose of this study is to propose a ratchet diagram for primary bending and secondary membrane loading conditions. For this, a finite element analysis model of a rectangular beam is prepared and solved by the numerical analysis software 'ABAQUS'. The FEA model is validated by carried out a dynamic nonlinear elastic-plastic analysis with the analytical solution of Yamashita et al. for similar loading conditions. The ratchet occurrence conditions plotted in a non-dimensional stress parameter plot similar to the Bree diagram. The findings suggest that secondary stress rises for the occurrence of ratchet conditions as primary stress decreases. It also found a strong frequency dependency feature. The nature of the input frequency of cyclic loading in the proposed ratchet diagram has been discussed in terms of dynamic displacement over static displacement in the change of non-dimensional frequency of the loading.

Keywords: Ratcheting; FEA; Membrane Loading; Bending Loading; Frequency Effect.

1. Introduction

Ratcheting is defined as the phenomenon where the cyclic accumulation of inelastic deformation occurs if the stress applied is high enough to make the structure yield due to a cyclic stressing with non-zero mean stress [1]. It is a special kind of cyclic deformation behavior that occurs in materials as well as structures where stresses are greater than the yield stress of the material [2]. Many types of engineering structures are subjected to cyclic loading. So, ratcheting is a key point that is considered during designing those structures for predicting safety and fatigue life of them, because there are many components where the combined effect of several applied stresses can exceed their yield stress. For those components, accurate prediction of ratcheting behavior is necessary as the wrong prediction can lead to a catastrophic failure. Under certain conditions, a correct combination of steady primary stress and cyclic thermal stress leads to ratcheting. This mechanism of ratcheting under cyclic thermal stress was investigated by Miller [3], Burgreen [4] and Bree [5]. From the Bree diagram, different loading sequences are found including steady thermal cyclic primary, in-phase cyclic thermal and primary stress, out-of-phase cyclic thermal and primary stress [6]. It is also found from the Bree diagram that steady thermal and cyclic primary stress is not accountable for ratcheting.

Ohno et al. [7] stated that "ratcheting happening under uniaxial cyclic loading with the non-zero mean stress is noted to uniaxial ratcheting, which is most fundamental and has been studied in many works". Cyclic tension is a very common phenomenon found in many engineering components. Under asymmetrical loading, the component faces cyclic creep. If cyclic load with a constant stress amplitude and non-zero mean stress is applied to the body, the total strain developed within the body becomes so large that the original shape of the structure may change. So uniaxial ratcheting can be a subject of further investigation especially when there are not lots of researchers worked on this particular topic.

In the present study, a ratchet diagram has been proposed for various combinations of primary bending and secondary membrane loading conditions. At first, a FEM model of a rectangular beam has been made and validated with the theoretical model proposed by Yamashita et al. [8] for similar loading conditions. Finally, when the ratchet occurrence condition has been obtained for various frequencies, the effect of frequency has been characterized and discussed.

2. Theory of ratcheting

Ratcheting is an important design criterion for the structures subjected to cyclic loadings. So, researches regarding the effects of ratcheting have been being done for a longer period of time. Researchers are trying to find out the effects caused by ratcheting on different materials and structures. Some of the relevant studies are important for the current study.

T. M. Mulcahy [9] investigated the effect name 'Bauschinger effect' with the help of thermal ratcheting upon a beam element. He investigated analytically for a beam element with a linear temperature variation across the solid cross-section of a rectangular beam. Finally, he tabulated specific results for materials and operating conditions associated with liquid metal breeder reactors.

T. H. Hyde, B. B. Sahari, and J. J. Webster [10] adopted the finite element method to investigate the behavior of thin tubes due to thermal ratcheting. The thin tubes were subjected to steady, internal pressure and cyclic, linear, through-thickness temperature distributions. They used an elastic-perfectly plastic material model for the analysis and related uniaxial behavior with multi-axial via von Mises yield criterion and Prandlt-Reuss flow rule. They found for an axially constrained tube that "if thermal loading is high enough then yielding occurs through the whole of the wall thickness simultaneously in each half cycle".

G.Z. Kang, Y.G. Li, J. Zhang, Y.F. Sun and Q. Gao [11] experimented on 25CDV4.11 steel and SS304 stainless steel for

ratcheting and failure behaviors under uniaxial cyclic tests. The experiment was conducted at room temperature. In the experiment, they first observed the cyclic hardening/softening features of the materials under uniaxial strain cycling. Finally, they observed for the ratcheting and failure behavior of those materials.

Md Abdullah Al Bari, Ryota Sakemi, Yamato Katsura and Naoto Kasahara [12] experimented with a rectangular beam under dynamic loading like seismic loading. They investigated for determining the conditions for the occurrence of ratcheting and collapse failure. The analogy between thermal ratcheting and dynamic ratcheting was considered in the analysis. A nonlinear dynamic finite element method was used to analyze the beam. Finally, they obtained experimental observations for ratcheting which they used to validate the analytical predictions and proposed a failure mode map.

K.S. Basaruddin and L.C. Wooi [13] experimentally investigated the uniaxial ratcheting characteristics of mild steel at room temperature. They conducted cyclic tension tests along with conventional monotonic, cyclic and ratcheting tests. Finally, they observed that "at the same stress amplitude (mean stress), the ratcheting strain increase as mean stress (stress amplitude) increased.

The simultaneous presence of constant primary stress and cyclic secondary stress in a uniaxial stress field can occur four types of ratcheting. Yamashita et al. [8] proposed a simplified evaluation method of ratcheting under primary bending and secondary membrane stress to develop an evaluation method for bending-membrane types of ratcheting. They calculated the dissipated energy of a beam due to bending-membrane loading using modified yield stress for the beam. They obtained that ratcheting will occur of a rectangular beam if

$$\frac{2X}{3} + \frac{Y}{2} > 1 \tag{1}$$

where X and Y are non-dimensional stress parameters [8]. Yamashita et al. proposed the following ratchet diagram (Fig. 1) by the analytical solution of a rectangular beam. Fig. 2 showed the loading and analysis condition of Yamashita et al.'s model.

There are other ratchet diagrams proposed for different loadings too. Ratchet diagram by Bree for membrane-bending loading conditions, Yamashita et al. [8] bending-bending theoretical ratchet diagram and subsequent numerical analysis of Bari et al. [12] are among them. The current study is based on the finite element analysis of Yamashita et al.'s theoretical bending-membrane ratchet model.

3. Methodology

In the current study, finite element analysis was used by numerical analysis software 'Abaqus'. The analysis conditions are shown in Table 1. The loading and constraint of the model are shown in Fig. 3. One end of the beam model was made fixed and at the other end movement along the vertical direction was restricted. The element type was chosen plane stress as the stress along thickness direction was insignificant. The elastic-perfectly plastic material model was used which is similar to Yamashita et al.'s theoretical model. In the ratcheting analysis, a rectangular beam of 140 mm in length, 13 mm in width and 6 mm in height was used.
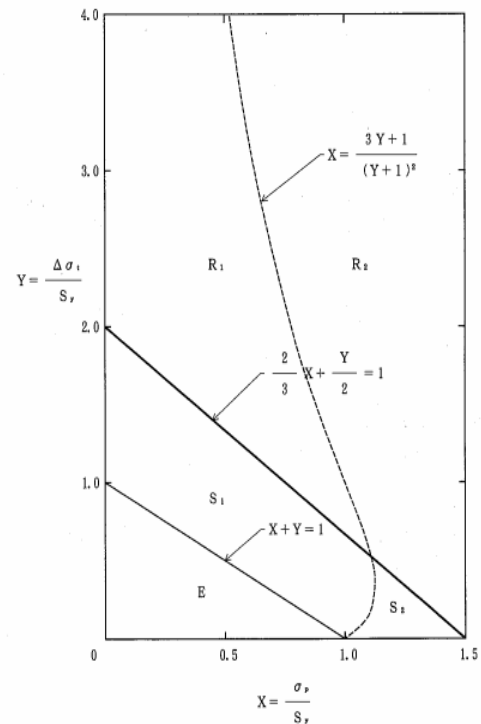
Fig. 1 Theoretical bending-membrane Ratchet diagram by Yamashita et al. [8]
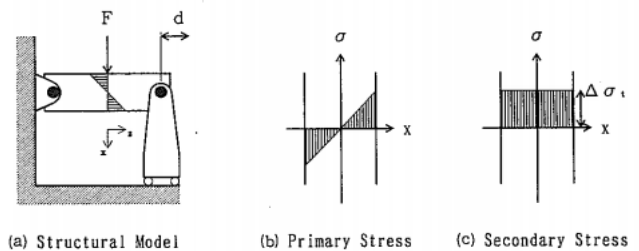
Fig. 2 Loading and analysis condition of Yamashita et al.'s theoretical model [8]

Table 1 Finite element analysis conditions

FEA platform	Abaqus ver.6.14
Analysis type	Dynamic elastic-plastic analysis with large deflection on
Element type	Plane stress (CPS4R)
Number of elements	2340
Input excitation	Displacement at the free end
Material properties	Lead (Pb)
	Density 11340 kg/m^3
	Young's modulus (E) 16 GPa
	Poisson's ratio 0.42
	Yield's stress 5 MPa
Material modeling	Elastic perfectly plastic
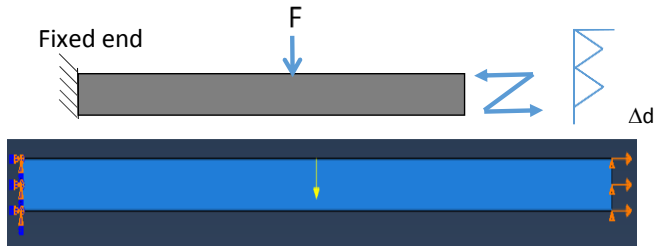
Fig. 3 Loading and constraint of the model

Ratcheting is observed under two loading conditions; primary and secondary loading. Primary loading is a load controlled loading and secondary loading is a displacement controlled loading. In this experiment, a concentrated load was used as primary loading and a cyclic displacement in axial direction was used as secondary loading similar to Yamashita's model. Concentrated load acts on the upper face of the beam. It acts downward along the midpoint of the beam. Displacement acts on the free end of the beam. It acts along the beam axis. A triangular shape of displacement was used with 10 cycles.

4. Results and discussions

Ratcheting can be understood from strain vs time diagram shown in Fig. 4. When ratcheting occurs, a gradual increase in strain is noticed in the diagram with time. If no gradual increase in strain with time is found, then it is evident that no ratcheting has occurred.
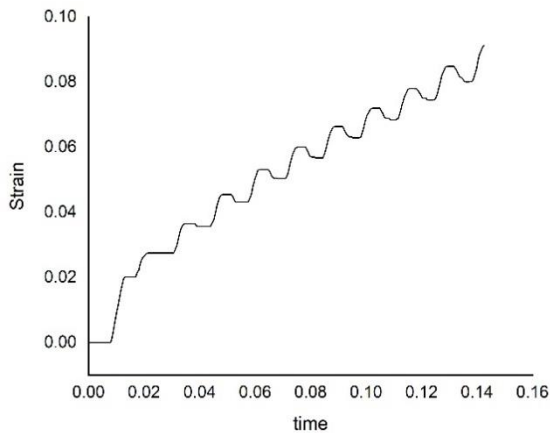

Fig. 4 Strain vs time diagram

As no experiment has been done in current research, so the numerical result is compared with Yamashita et al.'s theoretical ratchet diagram for validation purposes and shown in Fig. 5. From the comparison, it had seen that the numerical result followed an almost similar trend to the theoretical results. But a little deviation was also found at several points. The maximum deviation found was about 5%.

The ratcheting occurrence condition has been determined for different frequencies and plotted in terms of non-dimensional stress parameter X, Y diagram. Here, X is the non-dimensional primary stress parameter that can be expressed as

$$X = \frac{\sigma^d}{S_y} \tag{2}$$

and Y is the non-dimensional secondary stress parameter that can be expressed as

$$Y = \frac{\sigma^m}{S_y} \tag{3}$$

Here σ^d is the bending stress due to concentrated load and σ^m is the bending stress due to secondary membrane load. S_y is the yield stress. In the diagram, f_n stands for the natural frequency of the beam. For example, $1.5f_n$ means the applied frequency is 1.5 times the natural frequency of the beam. The stresses σ^d and σ^m is calculated by using the beam formula. Like the bending stress is calculated by using the following formula

$$\sigma^d = \frac{3Fl}{bh^2} \tag{4}$$

where F is the applied concentrated load, l is the length of the beam and b, h stands for beam width and height correspondingly.
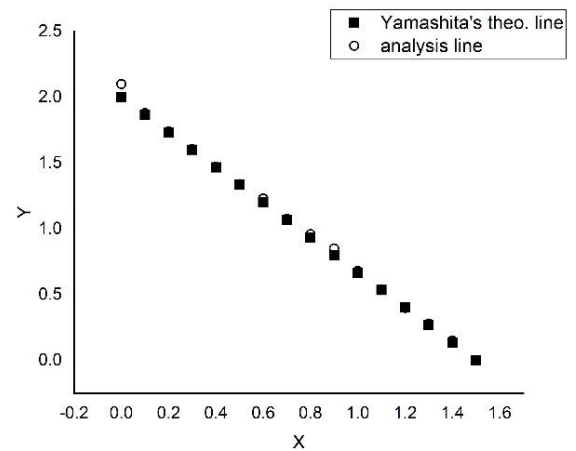
Fig. 5 Validation of numerical model with the theoretical model

The non-dimensional primary stress parameter X in the proposed ratchet diagram was plotted in abscissa, and the non-dimensional secondary stress parameter Y was plotted in ordinate. The X values varied from 0.4 to 1.5 and Y was varied to find the state of ratchet occurrence condition for every X values. By changing the concentrated force F, the X values were varied, and Table 2 displayed the corresponding X values for concentrated force F.

Table 2 Forces corresponding to the values of X

F (N)	X
2.229	0.4
3.343	0.6
4.457	0.8
5.5714	1.0
6.686	1.2
7.8	1.4

After getting the X and corresponding Y values, a ratchet diagram is plotted in Fig. 6. This ratchet diagram was plotted for natural frequency, which means the frequency of input secondary loading was the same as the natural frequency of the beam. From this graph, it has shown that Y decreases as X increases, but the graph's slope has been varied in various regions.

13
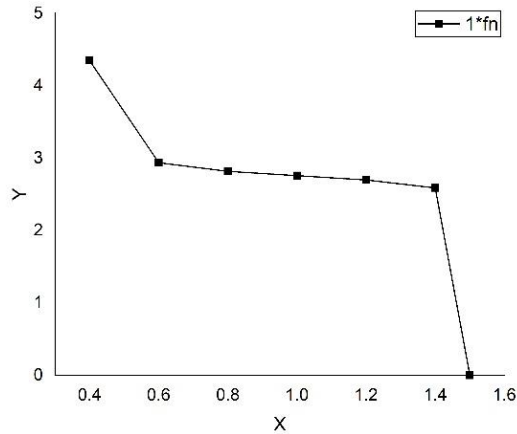
Fig. 6 Non-dimensional ratchet diagram for natural frequency

After completing the ratchet analysis and plotting all data in a non-dimensional stress plot similar to Yamashita's model, the final proposed ratchet diagram is obtained.
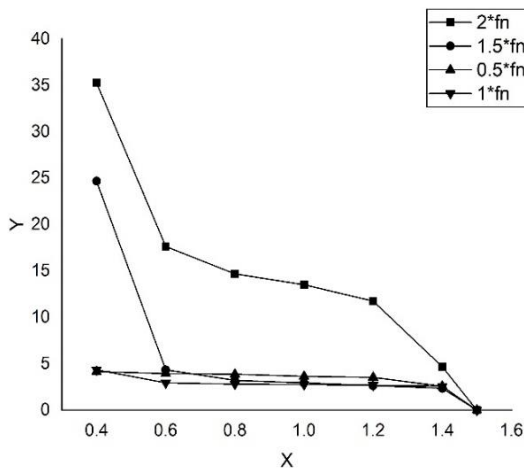
Fig. 7 Proposed ratchet diagram for bending-membrane loading conditions

In the proposed ratchet diagram, different lines representing the ratchet occurrence condition at different applied frequencies. Fig. 7 shows similar patterns of ratchet occurrence conditions as Yamashita et al.'s ratchet diagram. From this figure, it has shown that the secondary stress varies considerably for different levels of frequency for the occurrence of ratchet for particular primary stress. It can be shown that the lowest line in the proposed ratchet diagram was for $1f_n$, for the same ratchet incidence conditions the outermost line was for $2f_n$ and other lines were for 0.5 & $1.5f_n$ lies between those two lines. So it can be said that, in the case of ratchet occurrence, there was a strong frequency effect.

The effect of frequency on ratcheting occurrence condition can be explained with the help of the amplification factor graph as shown in Fig. 8. The plot's horizontal axis represents the non-dimensional frequency that is obtained by dividing the frequency of input by the normal beam frequency. The vertical axis represents the dynamic displacement over static displacement, which in other words, the amplification of displacement due to dynamic loading. From the amplification

factor graph, there are three distinct regions can be observed. It is evident that dynamic displacement and static displacement were almost the same for non-dimensional frequency range 0.25-0.5. From the plotting, the dynamic displacement increases when the frequency range increases from 0.5 and becomes maximum at the value of 1.0 which is called the resonance region. At the resonance region, a sudden increase in displacement was found. This sudden increase of displacement indicated that at natural frequency dynamic loading amplified and due to this, a small secondary loading could enough to cause ratcheting and that was why the lowermost line in the ratchet diagram was for natural frequency. On the other hand for higher non-dimensional frequency range, dynamic displacement decreases gradually and after 1.5 non-dimensional frequency, lower values of dynamic displacement were found and due to this, the effect of dynamic loading decreases at this frequency ranges. Because of this effect, the outermost lines in the ratchet diagram were for higher frequencies.
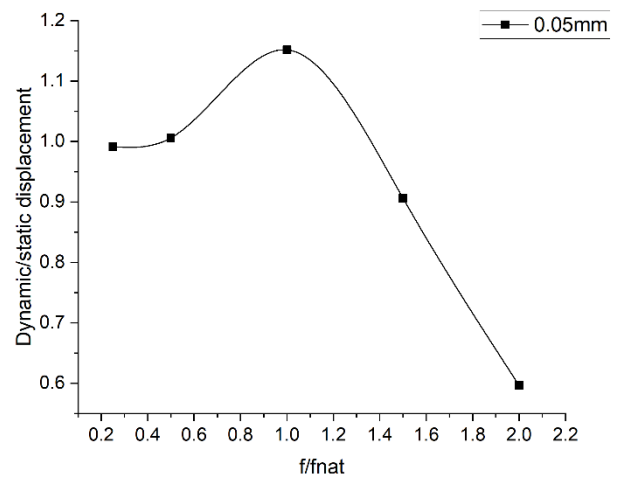
Fig. 8 Amplification factor graph

5. Conclusion

In this study, a dynamic non-linear elastic-plastic analysis was carried out on a rectangular beam for bending-membrane loading conditions. An FEA model was prepared and validated by Yamashita et al.'s analytical result. The analytical and numerical results showed a reasonable degree of agreement. The numerical model has then been used to propose a ratchet diagram for bending-membrane loading conditions and to investigate the effects of the frequency of input cyclic loading on ratchet occurrence. Finally, a ratchet diagram has been proposed for bending-membrane loading conditions. The Frequency dependency characteristics have also been observed in the ratchet diagram. The frequency effect was analyzed by the amplification factor graph and it has been found that the natural frequency was more dangerous and higher frequencies were safer for the structure in terms of ratcheting.

References

[1] Chen X, Chen X, Yu D, Gao B. Recent progresses in experimental investigation and finite element analysis of ratcheting in pressurized piping. International Journal of Pressure Vessels and Piping. 2013 Jan 1;101:113-42.

[2] Shariati M, Hatami H, Yarahmadi H, Eipakchi HR. An experimental study on the ratcheting and fatigue behavior of polyacetal under uniaxial cyclic loading. Materials & Design. 2012 Feb 1;34:302-12.

[3] Miller DR. Thermal-stress ratchet mechanism in pressure vessels. Journal of Basic Engineering. 1959 Jun 1;81(2):190-4.

[4] Burgreen D. Structural growth induced by thermal cycling. Journal of Fluid Engineering. 1968 December; 90(4): 469-75.

[5] Bree J. Elastic-plastic behaviour of thin tubes subjected to internal pressure and intermittent high-heat fluxes with application to fast-nuclear-reactor fuel elements. Journal of strain analysis. 1967 Jul 1;2(3):226-38.

[6] Ng HW, Moreton DN. Bree diagrams for alternative loading sequences(for identifying boundaries of strain behavior in thermal and pressure loading). Engineering approaches to high temperature design(A 84-37877 17-39). Swansea, Wales, Pineridge Press, 1983,. 1983:279-312.

[7] Mizuno M, Mima Y, Abdel-Karim M, Ohno N. Uniaxial ratchetting of 316FR steel at room temperature—Part I: experiments. J. Eng. Mater. Technol.. 2000 Jan 1;122(1):29-34..

[8] Yamashita T, Tsukimori K, Nagata T. Development of the simplified evaluation method for ratchetting due to primary bending stress and secondary membrane stress. Commercial Property. PNC ZN9410. 1992 May: 92-139.

[9] Mulcahy TM. Thermal ratcheting of a beam element having an idealized bauschinger effect. Journal of Engineering Materials and Technology, 98(3). 1976 July: 264-71.

[10] Hyde TH, Sahari BB, Webster JJ. The effect of axial loading and axial restraint on the thermal ratchetting of thin tubes. International journal of mechanical sciences. 1985 Jan 1;27(10):679-92.

[11] Kang GZ, Li YG, Zhang J, Sun YF, Gao Q. Uniaxial ratcheting and failure behaviors of two steels. Theoretical and Applied Fracture Mechanics. 2005 May 1;43(2):199-209.

[12] Al Bari MA, Sakemi R, Katsura Y, Kasahara N. Proposal of Failure Mode Map Under Dynamic Loading—Ratcheting and Collapse. Journal of Pressure Vessel Technology. 2018 Oct 1;140(5).

[13] Basaruddin KS, Wooi LC. Uniaxial ratcheting of mild steel under cyclic tension. In International Conference on Applications and Design in Mechanical Engineering (ICADME), Batu Ferringhi, Penang, Malaysia 2009 Oct (pp. 6E-1 -4).

Performance Analysis of a Heat Pipe with Stainless Steel Wick

Md Enamul Haque[1], Md Efthakher Hossain[2] and Mohammad Mashud[2]

[1]Department of Mechanical Engineering, Konya Technical University, Konya, Turkey
[2]Department of Mechanical Engineering, Khulna University of Engineering & Technology, Khulna-9203, BANGLADESH

ABSTRACT

In this study, the influences of different parameters on performance of a heat pipe with stainless steel net as wick have been presented. Experiments have been carried out for an input power range from 80 W to 160 W, constant cooling water mass flow rate of 0.0515 liter/s, and constant temperature at the inlet to condenser of 11°C. The temperatures were recorded at different power level by using a laser thermometer of the heater block, evaporator and condenser end at 50 second interval. Variation in the input power was done by varying the input voltage. It was done by a variack. Considering all criteria the copper is selected as the material of the container, water is selected as the working fluid of the heat pipe, stainless steel net is used as wick material. As copper/water heat pipes are able to tolerate storage temperatures between -65°C and 250°C, and can effectively operate between 10°C and 250°C. So a .9144 m copper tube is used to construct the heat pipe. Inside this tube stainless steel net is used as wick material to aid the flow of fluid. In the observation it is observed that the temperature of the evaporator end increases at a greater rate of the copper pipe than the heat pipe at different power level. It has been shown the variation of temperature of the heater block and the evaporator section at 80V, 100V, 120V, 140V, 160V respectively of the heat pipe and copper pipe.

Keywords: Heat Transfer; Stainless Steel Net; Copper Heat Pipe; Water Heat Pipe.

1. Introduction

The concept of heat pipes was introduced by R.S. Gaugler in 1940's. But, it was in 1984 that Cotter first introduced the idea of "micro" heat pipes [1]. Transportation of heat is one of the most difficult and inefficient tasks in thermal management [2]. It often results in costly heat transfer losses and reduced overall efficiency [3]. The performance of various mechanical and electrical components depends on the performance of the cooling system, because during operation they generate heat and dissipation of this heat is necessary for their optimum and reliable operation [2]. Many of today's electronic devices require cooling beyond the capabilities of standard metallic heat sinks. Cooling problems in micro electric circuits are generally critical because the generated heat must be dissipated from such small surface areas [4]. Heat transfer by heat pipes is one of the fastest and most efficient methods for thermal management. They offer a high efficiency, passive, compact heat transfer solution and are rapidly becoming a mainstream thermal management tool [5].

2. Historical Background of Heat Pipe

The development of the heat pipe originally started with Angier March Perkins who worked initially with the concept of the working fluid only in one phase [8]. Jacob Perkins patented the Perkins Tube in 1936 and they became widespread for use in locomotive boilers and baking ovens. The Perkins Tube was the jumping off point for the development of the modern heat pipe. The concept of the modern heat pipe, which relied on a wicking system to transport the liquid against gravity and up to the condenser, was put forward by R.S. Gaugler of the General Motors Corporation in 1942 [1]. In 1944, Gaugler described how his heat pipe would be applied to refrigeration systems. Heat pipe

research became popular after that and many industries and labs including Los Alamos, RCA, the Joint Nuclear Research Centre in Italy, began to apply heat pipe technology their fields. They have been a subject since the early1950s and are commercially available in a variety of forms [6]. In 1963 George Grover, an engineer of Los Alamos National Research Laboratory, demonstrated the first heat pipe. By 1969, there was a vast amount of interest on the part of NASA, Hughes, the European Space Agency, and other aircraft companies in regulating the temperature of a spacecraft and how that could be done with the help of heat pipes [9]. There has been extensive research done to date regarding specific heat transfer characteristics, in addition to the analysis of various material properties and geometries [8]-[10].

3. Working Principle of Heat Pipe

A heat pipe broadly divided in three sections namely, evaporator, adiabatic and condenser [7]. Heat pipes employ evaporative cooling to transfer thermal energy from one point to another by the evaporation and condensation of a working fluid or coolant. Heat pipes rely on a temperature difference between the ends of the pipe [2]. When one end of the heat pipe is heated the working fluid inside the pipe at that end evaporates and increases the vapor pressure inside the cavity of the heat pipe [4]. The latent heat of evaporation absorbed by the vaporization of the working fluid reduces the temperature at the hot end of the pipe .The vapor pressure over the hot liquid working fluid at the hot end of the pipe is higher than the equilibrium vapor pressure over condensing working fluid at the cooler end of the pipe, and this pressure difference drives a rapid mass transfer to the

condensing end where the excess vapor releases its latent heat, warming the cool end of the pipe [4]. The condensed working fluid then flows back to the hot end of the pipe, either by force of gravity in the case of vertically oriented heat pipes, or through capillary action in the case of heat pipes containing wicks, or heat pipes that are orientated horizontally relative to gravity. In summary inside a heat pipe "hot" vapor flows in one direction, condenses to the liquid phase which flows back in the other direction to evaporate again and close the cycle.
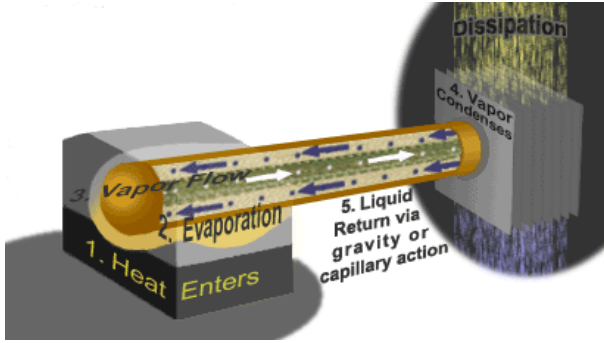

Fig. 1 Working principle of Heat Pipe [4]

4. Performance Evaluation

The performance evaluation of a heat pipe is necessary step that has to be often repeated in order to characterize many factors such as working temperature and maximum heat transfer capacity. The heat pipe performance is usually defined in terms of the temperature drop across the working length of heat pipe at a given power level. If Q is the heat load on the system and ΔT is the temperature drop across the heat pipe then the resistance R is the given by [5],

$$R = \frac{\Delta T}{Q}$$

The relation shown in the above equation is a derivative of the classic conduction equation,

$$Q = \frac{K \cdot A \cdot \Delta T}{L}$$

It is clear that resistance R is defined as,

$$R = \frac{L}{K \cdot A}$$

During this work the heat pipe performance was performance was measured in terms of conductance. In a way this measured quantity is similar to material thermal conductivity.

5. Design Considerations

Heat pipes must be tuned to particular cooling conditions. The choice of pipe material, size and coolant all have an effect on the optimal temperatures in which heat pipes work.

The three basic components of a heat pipe are:
Container, working fluid, wick or capillary structure [2].

To construct a heat pipe the following steps have to be followed**:**

(i). Determination of the working fluid appropriate for the application.

(ii). Selection of the pipe material compatible to the working fluid.

(ii). Selection of the wick structure for the operating orientation.

Table 1 Typical Operating Characteristics of Heat Pipes [20]

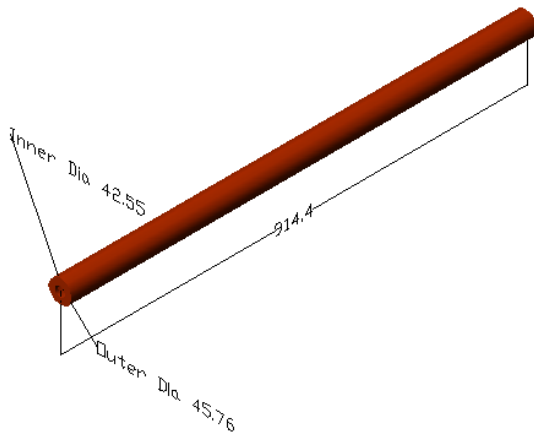| Temperature Range (°C)	Working Fluid	Vessel Material	Measured axial8 heat flux (kW/cm2)	Measured surface8 heat flux (W/ cm2)
-200 to -80	Liquid Nitrogen	Stainless Steel	0.067 @ -163°C	1.01 @ -16°3C
-70 to +60	Liquid Ammonia	Nickel, Aluminum, Stainless Steel	0.295	2.95
-45 to +120	Methanol Copper, Nickel, Stainless Steel	Copper, Nickel, Stainless Steel	0.45 @ 100°Cx	75.5 @ 100°C
+5 to +230	Water	Copper, Nickel	0.67 @ 200°C	146@ 170°C
+190 to +550	Mercury* +0.02% Magnesium +0.001%	Stainless Steel	25.1 @ 360°C*	181 @ 750°C
+400 to +800	Potassium*	Nickel, Stainless Steel	5.6 @ 750°C	181 @ 750°C
+500 to +900	Sodium*	Nickel, Stainless Steel	9.3 @ 850°C	224 @ 76°0C
+900 to +1,500	Lithium*	Niobium +1% Zirconium	2.0 @ 1250°C	207 @ 1250°C
1,500 + 2,000	Silver	Tantalum +5% Tungsten	4.1	413

5.1 Container

The function of the container is to isolate the working fluid from the outside environment. It has to therefore be leak-proof, maintain the pressure differential across its walls, and enable transfer of heat to take place from and into the working fluid. Selection of the container material depends on many factors. These are as follows [4]:

- Compatibility (both with working fluid and external environment)
- Strength to weight ratio
- Thermal conductivity
- Ease of fabrication, including welding, machine ability and ductility
- Porosity
- Wet ability

Most of the above are self-explanatory. A high strength to weight ratio is more important in spacecraft applications. The material should be non-porous to prevent the diffusion of vapor. A high thermal conductivity ensures minimum temperature drop between the heat source and the wick [9].

Considering the criteria, described above and from the table for the temperature range 5°C to 230°C [11], we select a copper as the material of the container.

Fig. 2 Container (all the dimensions are in millimeter)

5.2 Working Fluid

A particular working fluid can only be functional at certain temperature ranges. Also, the particular working fluid needs a compatible vessel material to prevent corrosion or chemical reaction between the fluid and the vessel. Corrosion will damage the vessel and chemical reaction can produce a non-condensable gas [12].

A first consideration in the identification of a suitable working fluid is the operating vapor temperature range. Within the approximate temperature band, several possible working fluids may exist, and a variety of characteristics must be examined in order to determine the most acceptable of these fluids for the application considered [12]-[13].

The prime requirements are:

- Compatibility with wick and wall materials
- Good thermal stability
- Wet ability of wick and wall materials
- Vapor pressure not too high or low over the operating temperature range
- High latent heat
- High thermal conductivity
- Low liquid and vapor viscosities
- High surface tension
- Acceptable freezing or pour point

The selection of the working fluid must also be based on thermodynamic considerations which are concerned with the various limitations to heat flow occurring within the heat pipe like, viscous, sonic, capillary, entrainment and nucleate boiling levels.

In heat pipe design, a high value of surface tension is desirable in order to enable the heat pipe to operate against gravity and to generate a high capillary driving force. In addition to high surface tension, it is necessary for the working fluid to wet the wick and the container material i.e. contact angle should be zero or very small. The vapor pressure over the operating temperature range must be sufficiently great to avoid high vapor velocities, which tend to setup large temperature gradient and cause flow instabilities.

A high latent heat of vaporization is desirable in order to transfer large amounts of heat with minimum fluid flow, and hence to maintain low pressure drops within the heat pipe. The thermal conductivity of the working fluid should preferably be high in order to minimize the radial temperature gradient and to reduce the possibility of nucleate boiling at the wick or wall surface. The resistance to fluid flow will be minimized by choosing fluids with low values of vapor and liquid viscosities.

Considering the criteria, described above and from the table for the temperature range 5°C to 230°C and for the copper container, water is selected as the working fluid of the Heat Pipe [14].

3.2.2.1 Amount of working fluid

Length of the evaporator, L = .1524 m
Radius of the cylinder, r =0.021275 m
Volume of the section V $=\pi r^2$L =.000086683m^3
So, the volume of working fluid, v = 0.086683 Ltr.

5.3 Wick or Capillary Structure

The wick provides the capillary driving force to return the condensate to the evaporator [1]. The quality and type of wick usually determines the performance of the heat pipe, for this is the heart of the product. Different types of wicks are used depending on the application for which the heat pipe is being used. It is a porous structure made of materials like steel, aluminum, nickel or copper in various ranges of pore sizes [2]. They are fabricated using metal foams, and more particularly felts, the latter being more frequently used. By varying the pressure on the felt during assembly, various pore sizes can be produced. By incorporating removable metal mandrels, an arterial structure can also be molded in the felt [16].

Fibrous materials, like ceramics, have also been used widely. They generally have smaller pores. The main disadvantage of ceramic fibers is that, they have little stiffness and usually require a continuous support by a metal mesh [3]. Thus while the fibre itself may be chemically compatible with the working fluids, the supporting materials may cause problems. More recently, interest has turned to carbon fibres as a wick material. Carbon fibre filaments have many fine longitudinal grooves on their surface, have high capillary pressures and are chemically stable. A number of heat pipes that have been successfully constructed using carbon fibre wicks seem to show a greater heat transport capability [17].

The prime purpose of the wick is to generate capillary pressure to transport the working fluid from the condenser to the evaporator. It must also be able to distribute the liquid around the evaporator section to any area where heat is likely to be received by the heat pipe. Often these two functions require wicks of different forms. The selection of the wick for a heat pipe depends on many factors, several of which are closely linked to the properties of the working fluid [17].

The maximum capillary head generated by a wick increases with decrease in pore size. The wick permeability increases with increasing pore size. Another feature of the wick, which must be optimized, is its thickness. The heat transport capability of the heat pipe is raised by increasing the wick thickness. The overall thermal resistance at the evaporator also depends on the conductivity of the working fluid in the wick. Other necessary properties of the wick are compatibility with the working fluid and wet ability. The most common types of

wicks that are used are Sintered Powder, Grooved Tube, and Screen Mesh etc [16].

For the construction of the heat pipe, considering above criteria and the temperature range, container material and working fluid, Stainless steel net is used as wick material.

5.4 Materials Used

- Copper pipe as container.
- Water as working fluid
- Stainless steel net as wick material.
- One aluminium pipe
- Two nipples.
- Two gate valves
- Mika
- Nicrome wire.
- Asbestos rope.
- Glass wool.
- Metal sheet.
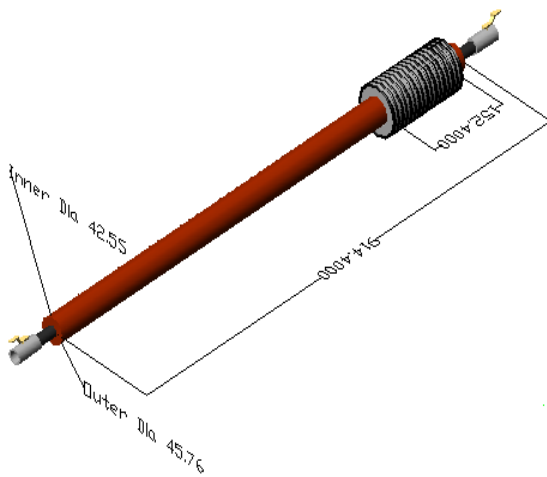
Fig. 3 Heat Pipe (All the dimensions are in millimeter)
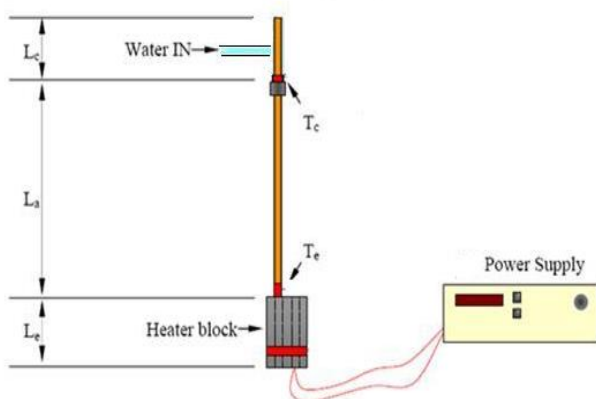
Fig. 4 Setup for Heat pipe's performance test

6. Construction Procedure

Heat pipes are generally composed of a tube, closed on each end, with fluid in it. As copper/water heat pipes are able to tolerate storage temperatures between -65°C and 250°C, and can effectively operate between 10°C and 250°C. So a .9144 m copper tube is used to construct the heat pipe. Inside this tube

stainless steel net is used as wick material to aid the flow of fluid. Water is used as working fluid. The two end of the tube are sealed by welding one copper sheet on each end of the tube. One small hole is made on each of the two sheets by drilling machine. One nipple is welled on each of the two holes. Then one get valve is placed on each nipple. One gate valve is connected with vacuumer and another valve is connected with a pipe which is submerged in the liquid filled beaker. A six inch aluminum tube is placed on one end of the copper tube. It works as the heater block. This tube is covered by mica to prevent passing of electricity from the heating coil to the aluminum tube as well as to the copper tube. Nicrome wire is used as heating coil which is spiraled through the aluminum tube. Then the coil is covered by mica and finally by asbestos rope. The coil is connected with wire through which electricity can pass through it. A certain portion of the copper pipe is covered with glass wool for preventing the transfer of heat.

7. Testing Procedure

The heat pipe was subjected to a heat load across its working length. The heater block was powered by electricity. Its power input was controlled by a regulated power supply. Heat was extracted by water. The flow rate and temperature of the supplied water was kept constant. The temperature of the supplied water was 11°C. The flow rate of the supplied water was .0515 Liter\Sec. The setup is shown in Fig. 4. Temperatures were recorded at different power level by using a laser thermometer of the heater block, evaporator and condenser end at 50 second interval. Variation in the input power was done by varying the input voltage. It was done by a variack.

7.1 Measurement Error and Losses

The measurement of thermal conductance is complicated by a number of other parameters not related to the physical state of the material. The nature of the test setup affects the data reduction due to various losses and leakages of the applied heat load. Thermal contact resistance is one of the major causes of heat loss in a test setup. It depends on factors such as pressure, surface roughness and hardness etc. Contact resistance comes into importance at two points in the setup, the contact between electrical heaters and heater block and contact resistance between heater block and the test subject.

The heat is transmitted across the interfacial contacts by conduction, through the air trapped in the gap and via radiation. Thermal resistance is caused by oxidation of contacting surfaces, and radiation heat transfer between microscopic voids due to surface roughness. Additionally, heat loss through the insulation also adds to the parasitic losses in the system. The heat supplied by the heaters, Q, is split into,

- $Q_{Heater\ block}$ =Heat dissipated by the heater block.
- $Q_{Insulation}$ =Heat loss through the insulation.
- $Q_{Adiabatic}$ =Heat loss through the adiabatic section.
- $Q_{Condenser}$ = Heat rejected to circulating water.

$Q= Q_{Heater\ block} +Q_{Insulation}+ Q_{Adiabatic}+ Q_{Condenser}$ [18]

Assuming that the condenser rejects all the heat to circulating water $Q_{Condenser}$ is the actual heat heat transferred through the heat pipe and all others are lost through the system. As shown in equation, since all of these are included in the

evaluation of heat pipe conductance, it introduces a corresponding error in recording of data.

The other factors that directly contribute to heat loss include errors in the measurement of input power and recorded temperatures. Also the variation in the temperature of cooling water is unpredictable. The changes in surrounding conditions increase or decrease the heat loss to the heat loss to the environment.

It is obvious that a number of such systematic errors are present in testing and that any reporting of thermal conductance of the heat pipe is subjective to the viewpoint of the person conducting test. Under such conditions, there is a possibility of disagreement in the results for tests conducted at different periods of time on the same test subject using the same test setup.

8. Results

Table 2 Results for Copper pipe

| Obs No	$\Delta T = T_1 - T_2$ (°C)	Voltage (v)	Current (A)	Power $P = v \times A$	Q (W)
1	36.1	80	5.38	430.4	1836.45
2	39	80	5.38	430.4	1981.89
3	42	80	5.38	430.4	2131.59
4	43.1	80	5.38	430.4	2184.19
5	41.9	80	5.38	430.4	2121.22
6	44.3	100	5.66	566	2240.51
7	50.9	100	5.66	566	2571.03
8	52.1	100	5.66	566	2630.09
9	56	100	5.66	566	2828.50
10	60.2	100	5.66	566	3034.08
11	64.8	120	5.95	714	3261.29
12	68	120	5.95	714	3419.16
13	71.4	120	5.95	714	3586.5
14	76.6	120	5.95	714	3843.55
15	81.2	120	5.95	714	40470.13
16	86.1	140	6.24	873.6	4309.82
17	88.6	140	6.24	873.6	4432.41
18	88	140	6.24	873.6	4400.81
19	88.2	140	6.24	873.6	4409.40
20	87.8	140	6.24	873.6	4387.17
21	88.9	160	6.59	1054.4	4437.20
22	94.5	160	6.59	1054.4	4705.79
23	95.5	160	6.59	1054.4	4748.1
24	96.9	160	6.59	1054.4	4808.79
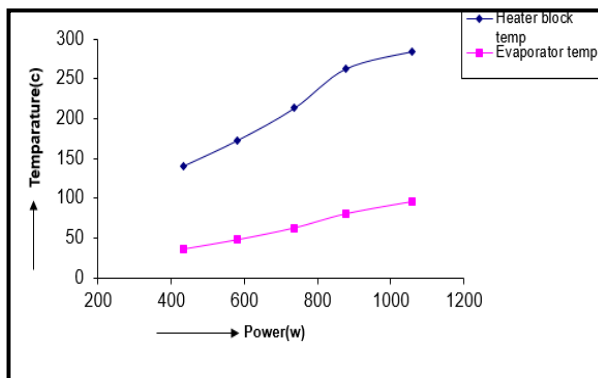
Fig. 5 Temperature Vs Power for Heat Pipe

Table 3 Results for Heat pipe

Obs No	$\Delta T = T_1 - T_2$ (°C)	Voltage (v)	Current (A)	Power $P = v \times A$	Q (W)
1	104	80	5.41	432.8	5264.75
2	107.9	80	5.41	432.8	5459.3
3	110.7	80	5.41	432.8	5598.89
4	116	80	5.41	432.8	5862.92
5	118.4	80	5.41	432.8	5982.33
6	124.6	100	5.82	582	6290.43
7	126.7	100	5.82	582	6394.67
8	129.7	100	5.82	582	6543.48
9	141.9	100	5.82	582	7147.32
10	141.7	100	5.82	582	7137.53
11	150.1	120	6.14	736.8	7552.22
12	153.2	120	6.14	736.8	7705.02
13	156.5	120	6.14	736.8	7842.1
14	161.6	120	6.14	736.8	7118.42
15	165.3	120	6.14	736.8	8302.31
16	163.4	140	6.26	876.4	8206.88
17	177.2	140	6.26	876.4	8883.86
18	181.6	140	6.26	876.4	9098.91
19	183	140	6.26	876.4	9167.34
20	187.9	140	6.26	876.4	9406.53
21	190	160	6.61	1057.6	9509.12
22	193	160	6.61	1057.6	9655.39
23	195.3	160	6.61	1057.6	9767.32
24	203.2	160	6.61	1057.6	10151.83
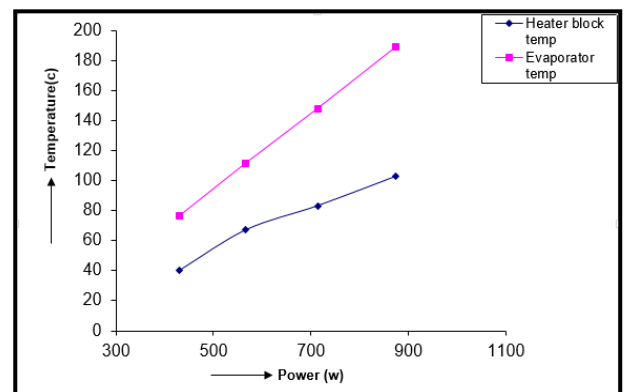
Fig. 6 Temperature Vs Power for Copper Pipe
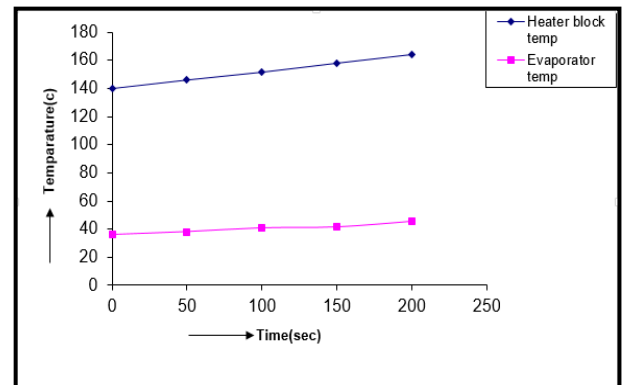
Fig. 7 Temperature Vs Time at 80V for Heat Pipe
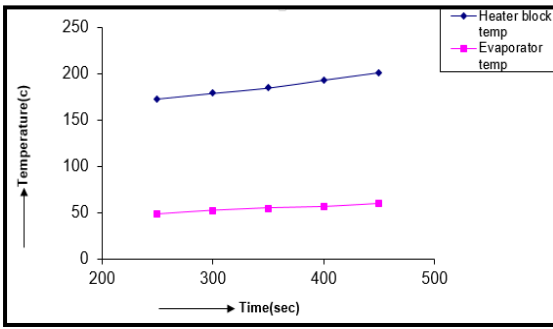
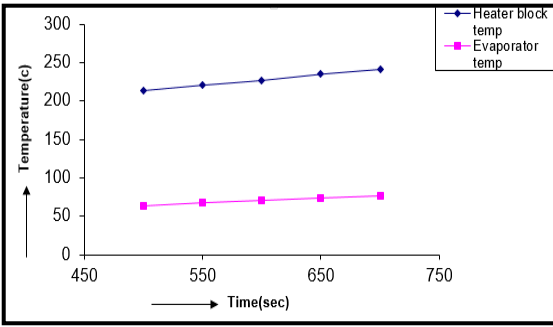**Fig. 8** Temperature Vs Time at 100V for Heat Pipe

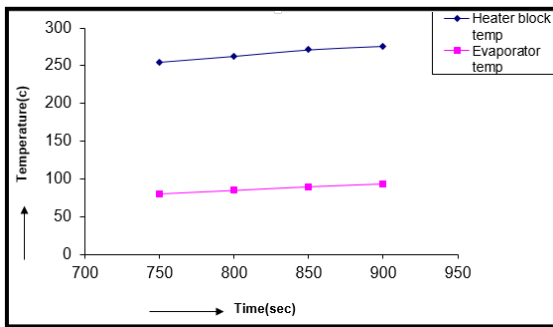**Fig. 9** Temperature Vs Time at 120V for Heat Pipe

Fig. 10 Temperature Vs Time at 140V for Heat Pipe
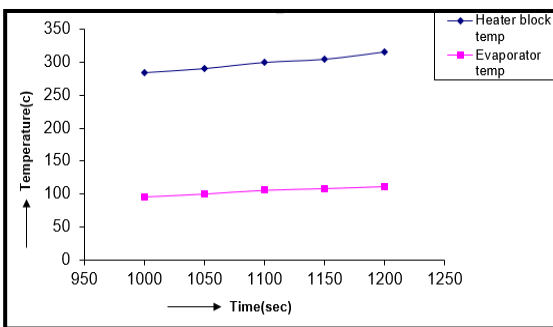

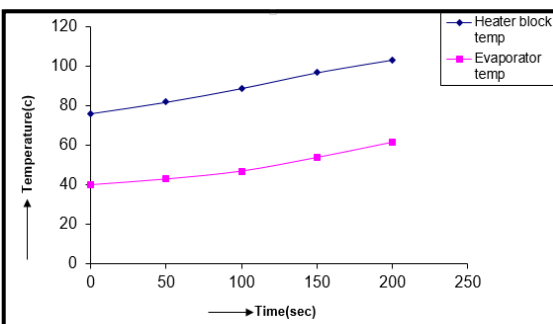**Fig. 11** Temperature Vs Time at 160V for Heat Pipe

Fig. 12 Temperature Vs Time at 80V for Copper Pipe
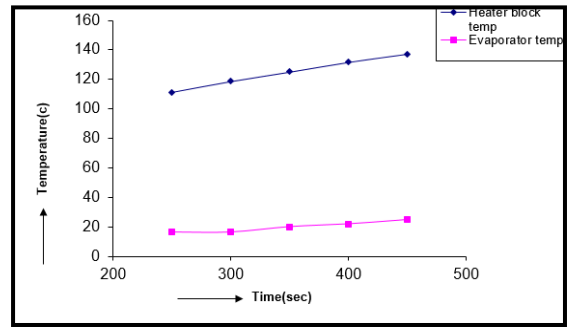

Fig. 13 Temperature Vs Time at 100V for Copper Pipe
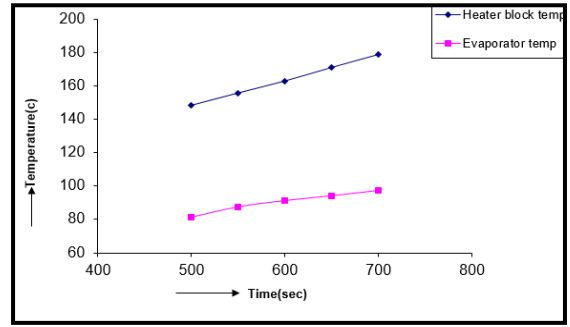

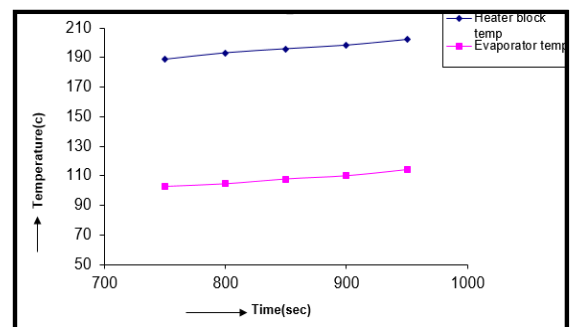**Fig. 14** Temperature Vs Time at 120V for Copper Pipe

Fig. 15 Temperature Vs Time at 140V for Copper Pipe
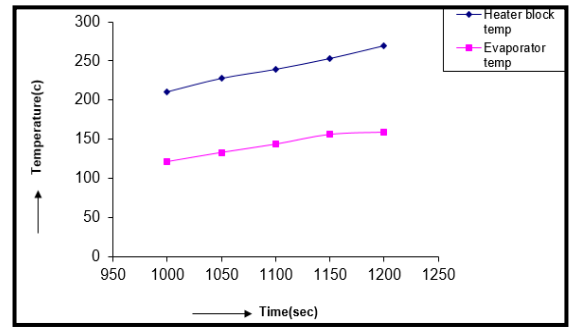
Fig. 16 Temperature Vs Time at 160V for Copper Pipe

9. Discussion

As it was necessary to vacuum the pipe perfectly for the best performance of the pipe that's why the pipe was sealed by gas welding. During this process the temperature was very high as a result the thermal characteristics of the wick material and the container were not remaining same. During the performance test the temperature was measured by laser thermometer as a result the temperature reading varies slightly. The rate of supplied cooling water was not uniform and the temperature of the supplied water varies as a result the value of temperature measured was not so accurate. From Fig. 5 & Fig. 6 it is observed that the temperature of the evaporator end increases

at a greater rate of the copper pipe than the heat pipe at different power level. Fig. 7-Fig. 11, shows the variation in temperature of the heater block and the evaporator section at 80V, 100V, 120V, 140V, 160V respectively of the heat pipe. Fig. 13-Fig. 16 shows the variation in temperature of the heater block and the evaporator section at 80V, 100V, 120V, 140V, 160V respectively of the copper pipe. From this fig it is observed that at same input voltage the rise in temperature of heater block and evaporator section of heat pipe is less than that of copper pipe. From the figures it is also clear that rate of increase in temperature at heater block and evaporator section is slower than that of the copper pipe.

10. Conclusion

During the performance test the cooling water was supplied by a long pipe which directly connected to the source. The cooling water directly strikes on the condenser end of the heat pipe and as the supplied water temperature was changed because of the change in ambient temperature. So if we can ensure a constant rate of supply and if the supplied water temperature remains constant then a better performance may be achieved. From literature review it is known that heat pipes have attracted a lot of attention over the years. The ongoing work on heat pipes made using sintered copper felt as the wicking medium was extended to explore the possibility of more efficient heat pipe.

Nomenclature

T	: Temperature, °C	L	: Length, m
W	: Power, Watt	D	: Diameter, m
t	: Time, second	A	: Area, m^2
Q	: Heat, Joule/sec	V	: Volume, m^3
V	: Voltage, Volt	K	: Coefficient of heat
A	: Current, Ampere	R	: Heat resistance

References

[1] Peterson GP. An introduction to heat pipes. Modeling, testing, and applications. Wiley Series in Thermal Management of Microelectronic and Electronic Systems, New York, Chichester: Wiley,| c1994. 1994.

[2] Odhekar DD, Harris DK. Experimental investigation of bendable heat pipes using sintered copper felt wick. InThermal and Thermomechanical Proceedings 10th Intersociety Conference on Phenomena in Electronics Systems, 2006. ITHERM 2006. 2006 May 30 (pp. 8-pp). IEEE.

[3] Mai T. *Attachment of Listeria Monocytogenes to Austenitic Stainless Steel* (Doctoral dissertation).

[4] Grady M. *Coaxial Probe for High Temperature Dielectric Characterization* (Doctoral dissertation).

[5] Ozisik MN. Heat transfer: a basic approach. New York: McGraw-Hill; 1985 Dec.

[6] Palkar A. *An Experimental Investigation of Liquid Metal MHPs* (Doctoral dissertation).

[7] Harris DK. "Experimental investigation of bendable heat pipes using sintered copper felt wick" , Thermal and Thermomechanical Proceedings 10th Intersociety Conference on Phenomena in Electronics Systems 2006 ITHERM 2006, 2006.

[8] Dunn PD, Reay DA. Heat pipes, 3rd ed. Oxford Oxfordshire ; New York: Pergamon Press, 1982.

[9] Peterson GP. Experimental investigation of micro heat pipes in silicon wafers. Micromechanical Sensors, Actuators, and Systems, ASME. 1991;32.

[10] Lai A, Gillot C, Ivanova M, Avenas Y, Louis C, Schaeffer C, Fournier E. Thermal characterization of flat silicon heat pipes. InTwentieth Annual IEEE Semiconductor Thermal Measurement and Management Symposium (IEEE Cat. No. 04CH37545) 2004 Mar 11 (pp. 21-25). IEEE.

[11] Dunn P, Reay DA. "Practical Design Considerations" , Elsevier BV, 1982.

[12] Ong KS, Hamlaoui A. Experimental Observations of Water-filled and R134a-filled Thermosyphons Operating at Low Temperatures. JOURNAL OF ENERGY HEAT AND MASS TRANSFER. 2002;24(3):235-54.

[13] Noie-Baghban SH, Majideian GR. Waste heat recovery using heat pipe heat exchanger (HPHE) for surgery rooms in hospitals. Applied thermal engineering. 2000 Oct 1;20(14):1271-82.

[14] Liang TS, Hung YM. Experimental investigation on the thermal performance and optimization of heat sink with U-shape heat pipes. Energy Conversion and Management. 2010 Nov 1;51(11):2109-16.

[15] Zohuri B. Heat pipe design and technology: Modern applications for practical thermal management. Springer; 2016 Apr 28.

[16] Semena MG, Zaripov VK. Investigation of the effective thermal conductivity of metal-fiber wicks in low-temperature heat pipes. Journal of engineering physics. 1977 Aug 1;33(2):911-6.

[17] Vasiliev LL, Kulakov AG, Filatova OS, Epifanov SV. Copper sintered powder wick structures of miniature heat pipes. InVI Minsk international seminar 'heat pipes, heat pumps, refrigerators. Minsk, Belarus 2005 Sep (pp. 12-15).

[18] Cengel YA. Introduction to thermodynamics and heat transfer, 1997. New York: MacGraw-Hill series in mechanical engineering.

[19] Wang Y, Han X, Liang Q, He W, Lang Z. Experimental investigation of the thermal performance of a novel concentric condenser heat pipe array. International Journal of Heat and Mass Transfer. 2015 Mar 1;82:170-8.

[20] Silverstein C. Design and technology of heat pipes for cooling and heat exchange. CRC press; 1992 Aug 1.

[21] Hossain ME. " Construction and Performance test of Heat Pipe" Department of Mechanical Engineering, Khulna University of Engineering & Technology, Bangladesh-2008.

Direct Numerical Simulation of Laminar Natural Convection in a Square Cavity at Different Inclination Angle

Mohammad Ilias Inam*

Department of Mechanical Engineering, Khulna University of Engineering & Technology, Khulna-9203, BANGLADESH

ABSTRACT

The effect of angle of rotation on laminar natural convection inside the square cavity have been observed in this research. It was assumed that left and right walls heated isothermally, whereas other two walls act as adiabatic. This problem was solved by assuming 2-D and by Direct Numerical Simulation (DNS) method using ANSYS Fluent 16.0. A series of DNS simulation were carried out for different inclination angle ($\theta = 0°{\sim}90°$) of the cavity at $Ra = 10^3$ & 10^4. It was observed that at average Nusselt number increase up to some value of angle of inclination after that it decrease though this variation is not significant.

Keywords: Natural Convection; Inclination Angle; Nusselt Number

1. Introduction

Study on natural convection heat transfer in square cavity have intense research interest due to its enormous engineering application like as building insulation, cooling devices for electronic instruments, nuclear reactor design and solar energy collectors etc. An extensive research have been conducted on this field by analytically, numerically and experimentally.

Natural heat transfer characteristics inside the enclosure is controlled by some parameter, like as shape of the enclosure, aspect ratio, Rayleigh number and angle of inclination etc. Extensive study have been conducted to understand the effect of shape, aspect ratio of enclosure. Numerical investigation of the heat transfer characteristics of two dimensional rectangular enclosure with isothermal boundary condition for different aspect ratio was studied by Churchill [1] and De Vahl Davis [2]. An extensive review of natural convection inside the enclosure (non-square) were carried out by Das *et al.* [3]. The fluid flow due to the induce buoyancy force becomes turbulent when Rayleigh number exceed by some critical values [4]-[6]. Effect of inclination of rectangular cavity on the natural convection was studied by Sharif and Liu [7] and Kuyper et al. [8]. They conducted their simulation at high Rayleigh number.

It is observed form the previous literature review that there is a lack of understanding about the effect of angle of inclination of square cavity at low Rayleigh number, which motivates for this research. For these reason, a series of two dimensional Direct Numerical Simulation (DNS) were carried for different angle of rotation ($\theta = 0°{\sim}90°$) of square cavity at low Rayleigh number ($Ra = 10^3$ & 10^4) using ANSYS Fluent 16.0.

2. Methodology

The physical system consider for this simulation is a two dimensional square enclosure with dimension ($100\ mm \times 100\ mm$), containing Newtonian fluid, sketched at Fig. 1. The left wall was consider as a rigid wall with constant temperature equal to 310K and right wall was consider as rigid wall with constant temperature equal to 300K. Other two walls were

assumed as adiabatic wall. To observe the effect of angle inclination on the natural convection in a rectangular square cavity, the gravitational direction was change during this simulation, instead of rotating the square cavity. For zero degree rotation ($\theta = 0°$), gravity was considered acting along the negative *y*-axis. However, for any arbitrary rotation θ, the component of gravitation forces were considered to be equal to $-g \sin \theta$ and $-g \cos \theta$ which is acting along *x*- axis and *y*-axis, respectively. During this simulation it was assumed that flow was steady, incompressible and two dimensional. Also Boussinesq approximation was considered during these DNS simulation run.
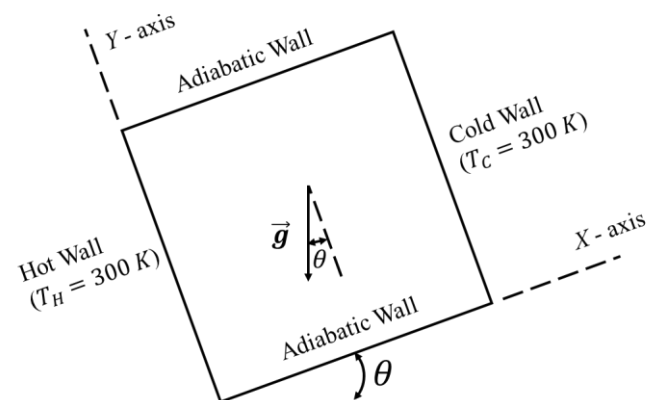

Fig. 1 Domain with boundary condition

The two dimensional governing equations (Continuity, Navier-Stokes equation and Energy equation) for these flow in Cartesian coordinates are written as follows:

$$\frac{\partial u}{\partial x} + \frac{\partial v}{\partial y} = 0 \tag{1}$$

$$u\frac{\partial u}{\partial x} + v\frac{\partial u}{\partial y} = -\frac{1}{\rho_{ref}}\frac{\partial P}{\partial x} + \vartheta\left(\frac{\partial^2 u}{\partial x^2} + \frac{\partial^2 v}{\partial y^2}\right) - \frac{\rho}{\rho_{ref}}g\sin\theta \tag{2}$$

$$u\frac{\partial v}{\partial x} + v\frac{\partial v}{\partial y} = -\frac{1}{\rho_{ref}}\frac{\partial P}{\partial y} + \vartheta\left(\frac{\partial^2 u}{\partial x^2} + \frac{\partial^2 v}{\partial y^2}\right) - \frac{\rho}{\rho_{ref}}g\cos\theta \tag{3}$$

$$u\frac{\partial T}{\partial x} + v\frac{\partial T}{\partial y} = \alpha\left(\frac{\partial^2 T}{\partial x^2} + \frac{\partial^2 T}{\partial y^2}\right) \qquad (4)$$

where u, v are the velocity component in the x and y direction, respectively. Also, kinematic viscosity and thermal diffusivity represent by ϑ and α, respectively.

The appropriate boundary conditions are:

Left wall: $u = v = 0 \,\&\, T = 310K$

Right wall: $u = v = 0 \,\&\, T = 300K$

Lower and upper wall: $u = v = 0 \,\&\, \frac{dT}{dy} = 0$

For these DNS simulations ANSYS Fluent 16.0 were used. ANSYS Fluent use finite volume method to discretize the above governing equations. Pressure based solver was used for these DNS simulation run. Also, SIMPLE scheme for pressure and velocity coupling; Green-Gauss cell based for gradient, PRESTO for pressure gradient and QUICK scheme for both momentum and energy equations.

In this paper, simulation were carried out for two different Rayleigh number ($Ra = 10^3 \,\&\, 10^4$), whereas this Rayleigh number is defined by the following equation:

$$Ra = \frac{g\beta(T_H - T_C)L^3}{\vartheta\alpha} \qquad (5)$$

Where, β is thermal expansion coefficient, L distance among hot and cold wall. For these simulation, consider air was the working fluid. The different value of Ra for these DNS simulation run was achieved by changing the value of gravitational acceleration, g. Also, Local Nusselt number, Nu, and average Nusselt number, Nu_{av}, were calculated with the following equations:

$$Nu = \frac{hL}{k} \qquad (6)$$

$$Nu_{av} = \frac{1}{L}\int_0^L Nu \, dy \qquad (7)$$

Where, h is the convection heat transfer coefficient and k is the thermal conductivity.

A non-uniform structural mesh was created with ANSYS mesh with higher resolution near to the wall, see Fig. 2. Specifically, for these mesh generation both horizontal and vertical wall were divided by 100 division with center biasing type with bias factor 10 to create fine mesh along the wall. This result was validated by comparing with previous date which is listed in

Table 1. Converging criteria was set for these simulation based on average Nusselt number (Nu_{av}) and simulation were run until this value of Nu_{av} to become a constant. Fig. 3 depicts variation of average Nusselt number (Nu_{av}) respect to number

of iteration for $Ra = 10^3$ for zero degree angle of rotation. It is observed from Figure that average Nusselt number (Nu_{av}) is changing significantly up to around 1000, after that it becomes almost stable with little variation and reach to a constant value which equal to 1.118 at around 1650 number iteration. Once the value of Nu_{av} reach to the constant value, this simulation were run for more number of iteration to ensure the steady nature of the result. It was observed from simulation that value of Nu_{av} reach to the constant value when the value of the residual of continuity equation, x-velocity, y-velocity and energy equation reach to around 10^{-8}, 10^{-8}, 10^{-8}, 10^{-13}, respectively. This procedure was followed for all the DNS runs carried out for this paper.
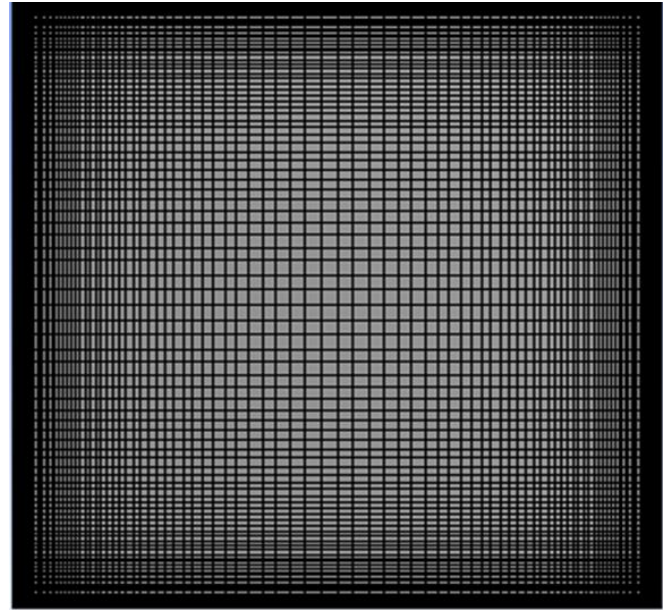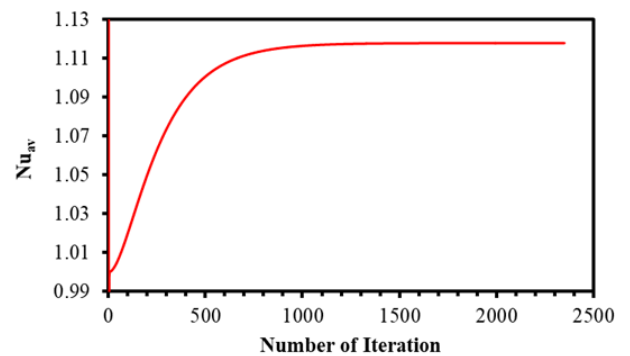

Fig. 2 Mesh used for these simulations

Fig. 3 Variation of average Nusselt number (Nu_{av}) with number of iteration at Ra = 10^3 & θ=0

Table 1 Comparison of present work with previous work for square cavity

	$Ra = 10^3$	$Ra = 10^4$	$Ra = 10^5$	$Ra = 10^6$
Present study	1.1179	2.2469	4.5347	8.8545
De Vahl Davis and Jones (1983)	1.118	2.243	4.519	8.799
A. Rincón-Casado et. al.	1.118	2.241	4.522	8.819

3. Results and Discussion

Fig. 4 depicts the temperature contour of the square cavity for different angle of rotation (θ) at $Ra = 10^3$. In this figure, temperature contour are shown without angle of inclination of the cavity. The exact position of the contour of the square cavity will be found by rotating anti-clock wise each contour shown in the figure with the value of θ is mention underneath of each figure. It is clearly observed form the figure that at $\theta = 0°$ at the top of the square cavity have higher temperature distribution for wider region compare to cooler region whereas in the bottom cooler region is wider than high temperature region. This result is expected due to the buoyancy effect. Fluid near to the left wall will rise due to the heating which reduce fluid density. Similarly, fluid density increase near to the right wall due to the cooling which produce a downward flow. Temperature distribution pattern are almost similar pattern for $\theta = 0°\sim70°$, whereas at $\theta = 80°\sim90°$ have different patter since gravitation force direction are almost perpendicular to the heating wall at $\theta = 80°\sim90°$, whereas it was parallel at $\theta = 0°$.

Fig. 5 shows temperature contour of the square cavity for different angle of rotation (θ) at $Ra = 10^4$. In this figure, temperature contour are also shown without angle of inclination of the square cavity. The exact position of the contour of the square cavity will be found similarly by rotating each contour shown in the figure with the value of θ is mention. It is clearly observed from figure that higher temperature zone is also wider in to top of square cavity and lower temperature zone is dominating at the bottom due to buoyancy effect which mention in the previous paragraph.

Fig. 6 depicts variation of local Nusselt number (Nu) along the heated wall (left side wall) at different angle of inclination (θ) for (a) $Ra = 10^3$ and (b) $Ra = 10^4$. It is clearly seen from Fig. 6 (a) for $Ra = 10^3$ at $\theta = 0°$ that Nu have higher value at the bottom of the heated wall which followed by slightly increase up to certain height and then starts to decrease and finally becomes almost constant near to the top of the wall. This similar behavior is also observed for other angle of inclination except $\theta = 90°$. The value of Nu is slightly higher at the lower side for $\theta = 20°$ which decrease at $\theta = 50°$ compare to $\theta = 0°$, however no significant difference is observed at the upper sider of the heated wall. For $\theta = 80°$, Nu significantly decrease at the bottom of the wall and increase at the top of the wall. In case of $\theta = 90°$, Nu is equal to one along the whole heated wall since gravitation force acts to the perpendicular direction to the heated wall. Similar behavior is also observe for $Re = 10^4$ for different angle of inclination except $\theta = 90°$, see Fig. 6 (b). For $\theta = 90°$ at $Re = 10^4$, Nu have lower value at the bottom of the wall and higher at the top of the wall whereas as opposite behavior is observed for other angle of inclination. This is also happen since gravitation force acting to the parallel to the heated wall at $\theta = 0°$ which is changing respect to the angle of inclination and becomes perpendicular at $\theta = 90°$.

(a) $\theta = 0°$ (b) $\theta = 5°$ (c) $\theta = 10°$ (d) $\theta = 15°$

(e) $\theta = 20°$ (f) $\theta = 30°$ (g) $\theta = 40°$ (h) $\theta = 50°$

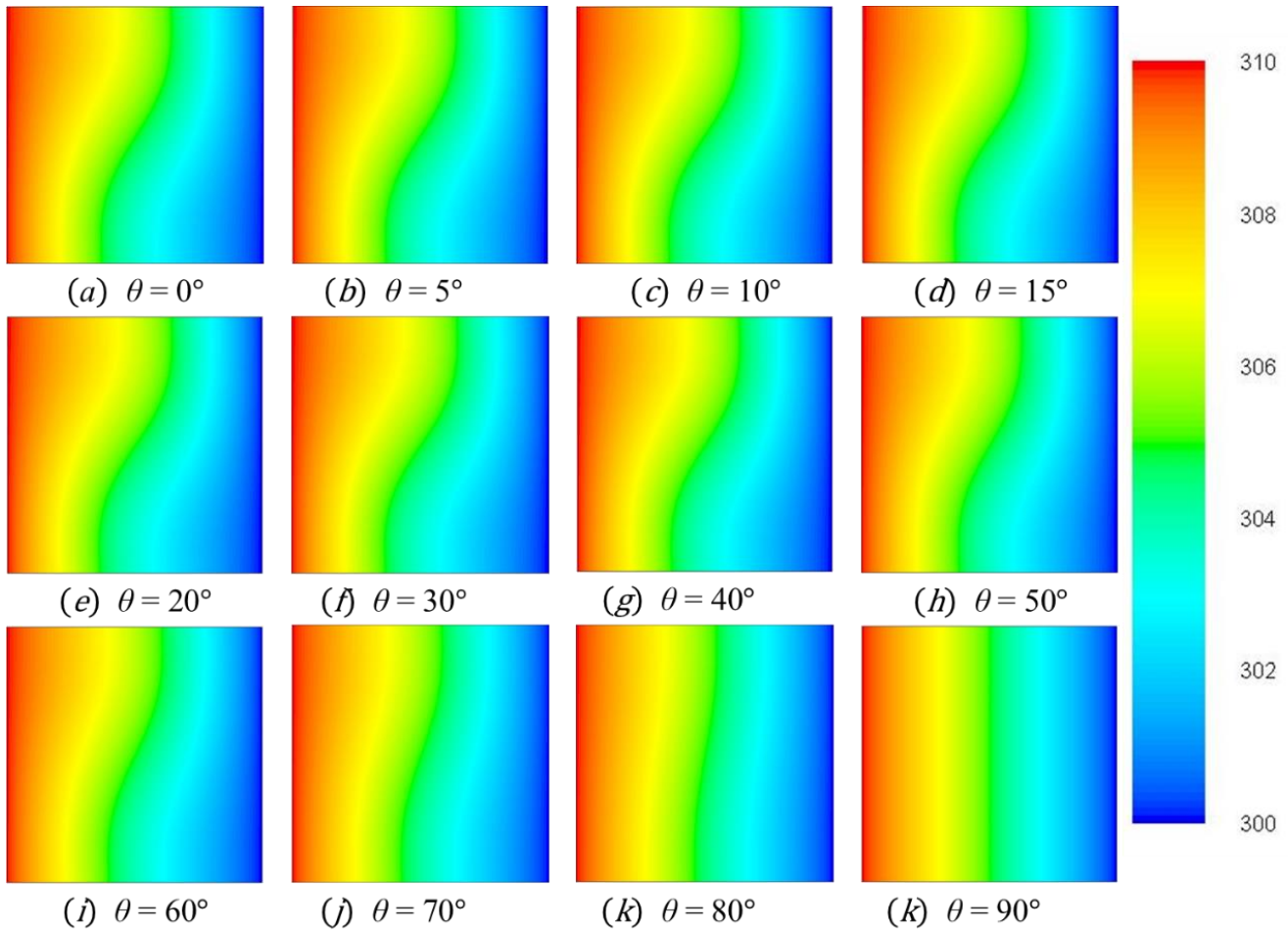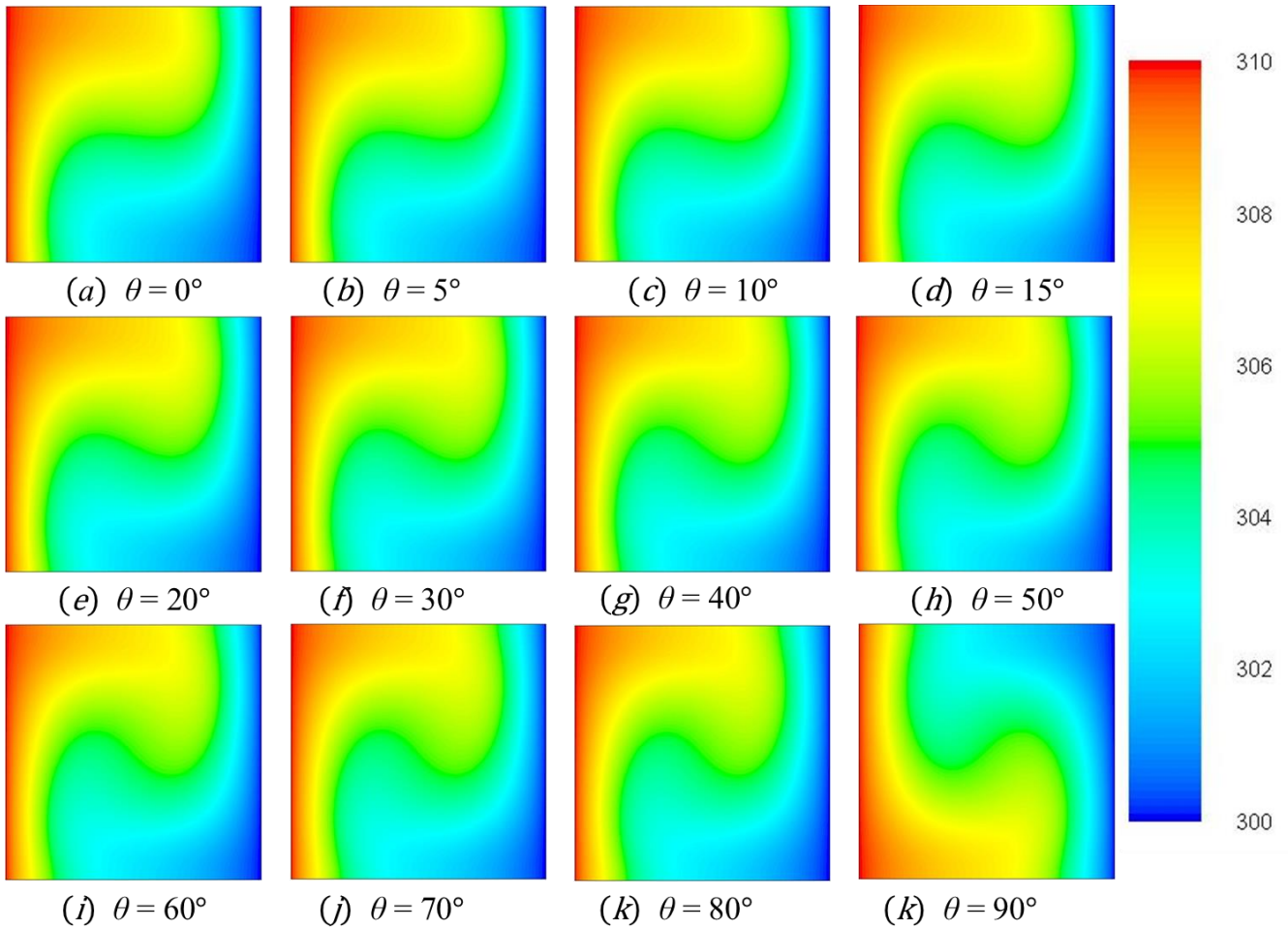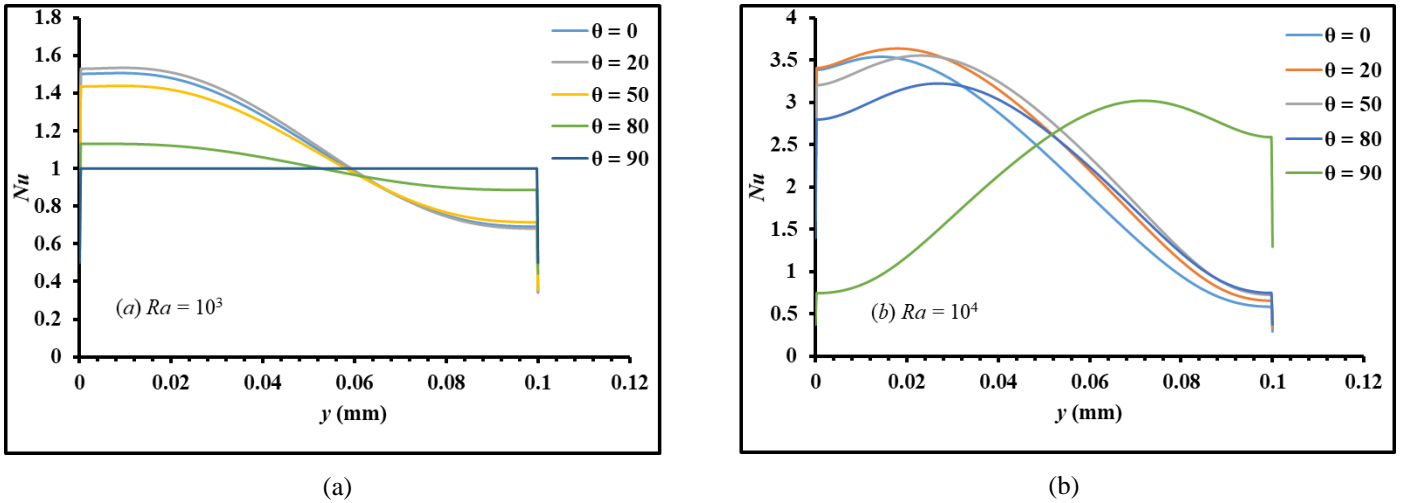(i) $\theta = 60°$ (j) $\theta = 70°$ (k) $\theta = 80°$ (k) $\theta = 90°$

Fig. 4 Temperature contour of the square cavity for different angle of rotation (θ) at Ra = 10^3

**Fig. 5** Temperature contour of inside the square cavity for different angle of rotation (θ) at Ra = 10^4

(a)

(b)

Fig. 6 Local Nusselt number (Nu) variation along the left wall (heated wall) at different angle of inclination (θ) for (a) Re = 10^3 and (b) Re = 10^4

Fig. 7 shows variation of average Nusselt number (Nu_{av}) respect to angle of inclination (θ) for $Re = 10^3$ and $Re = 10^4$. It is clearly observed from figure that Nu_{av} increase up to some angle of rotation than again decrease. For $Re = 10^3$, see Fig. 7 (a), Nu_{av} increase up to $\theta = 20°$ by around 1.15% after that is decrease nonlinearly up to $\theta = 90°$ and reach to the unit value of average Nusselt number. When $Re = 10^4$, see Fig. 7 (b), Nu_{av} also increase up to $\theta = 40°$ by around 10.63% after that is decrease nonlinearly up to $\theta = 90°$.

(a)

(b)
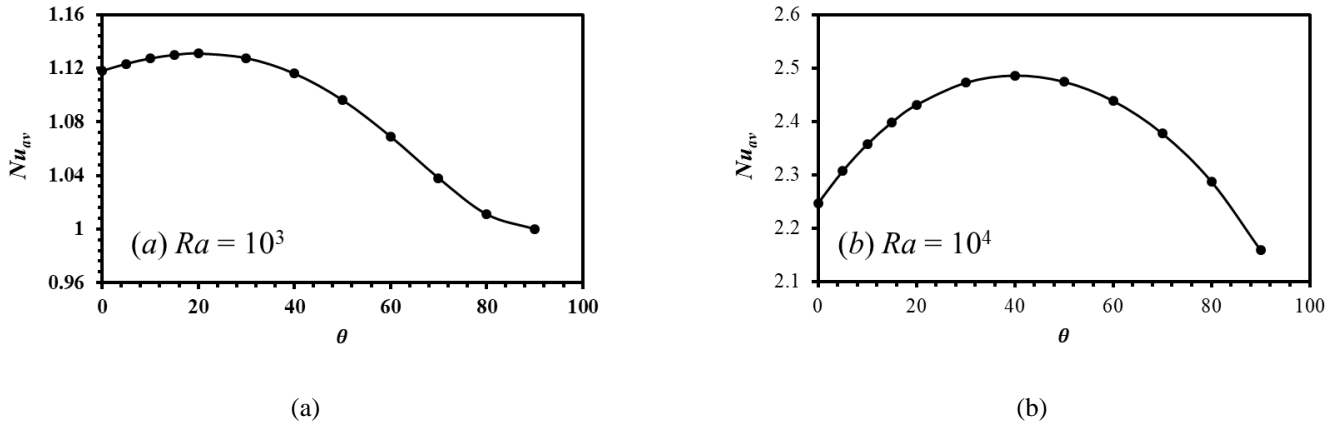
Fig. 7 Effect of angle of rotation (θ) on the average Nusselt number (Nu_{av}) at (a) Ra = 10^3 and (b) Ra = 10^4

4. Conclusion

This paper presents the effect of angle of orientation on the laminar natural convection inside a square cavity by DNS. It is observed that angle of orientation has positive effect on Average Nusselt number up to certain value, like as up to $\boldsymbol{\theta} = \boldsymbol{20°}$ for $Re = 10^3$ and $\boldsymbol{\theta} = \boldsymbol{40°}$ for $Re = 10^4$. Later on it decrease with increasing angle of orientation. However, the effect of angle of orientation of cavity has not much significant effect on Average Nusselt number.

References

[1] Wilkes JO, Churchill SW. The finite-difference computation of natural convection in a rectangular enclosure. AIChE Journal. 1966 Jan;12(1):161-6.

[2] de Vahl Davis G. Laminar natural convection in an enclosed rectangular cavity. International Journal of Heat and Mass Transfer. 1968 Nov 1;11(11):1675-93.

[3] Das D, Roy M, Basak T. Studies on natural convection within enclosures of various (non-square) shapes–A review. International Journal of Heat and Mass Transfer. 2017 Mar 1;106:356-406.

[4] Townsend AA. The structure of turbulent shear flow. Cambridge university press; 1980 Mar 6.

[5] Lesieur M. Turbulence in fluids: stochastic and numerical modelling. Boston, MA: Nijhoff; 1987 Jan 1.

[6] Foias C, Manley O, Rosa R, Temam R. Navier-Stokes equations and turbulence. Cambridge University Press; 2001 Aug 27.

[7] Foias C, Manley O, Rosa R, Temam R. Navier-Stokes equations and turbulence. Cambridge University Press; 2001 Aug 27.

[8] Sharif MA, Liu W. Numerical study of turbulent natural convection in a side-heated square cavityat various angles of inclination. Numerical Heat Transfer: Part A: Applications. 2003 May 1;43(7):693-716.

Indexed by:

Google Scholar

Crossref